Ab initio molecular-dynamics simulation of the liquid-metal–amorphous-semiconductor transition in germanium

G. Kresse and J. Hafner
Institut für Theoretische Physik, Technische Universität Wien, Wiedner Hauptstraße 8–10, A-1040 Wien, Austria
(Received 16 December 1993)

We present *ab initio* quantum-mechanical molecular-dynamics simulations of the liquid-metal–amorphous-semiconductor transition in Ge. Our simulations are based on (a) finite-temperature density-functional theory of the one-electron states, (b) exact energy minimization and hence calculation of the exact Hellmann-Feynman forces after each molecular-dynamics step using preconditioned conjugate-gradient techniques, (c) accurate nonlocal pseudopotentials, and (d) Nosé dynamics for generating a canonical ensemble. This method gives perfect control of the adiabaticity of the electron-ion ensemble and allows us to perform simulations over more than 30 ps. The computer-generated ensemble describes the structural, dynamic, and electronic properties of liquid and amorphous Ge in very good agreement with experiment. The simulation allows us to study in detail the changes in the structure-property relationship through the metal-semiconductor transition. We report a detailed analysis of the local structural properties and their changes induced by an annealing process. The geometrical, bonding, and spectral properties of defects in the disordered tetrahedral network are investigated and compared with experiment.

I. INTRODUCTION

Amorphous materials are of interest in materials science on both the basic and technological levels. Particularly challenging are the structural properties of these materials which have been the subject of numerous experimental and theoretical studies and controversy.[1] For a crystalline structure, the complete set of atomic coordinates may be derived from diffraction experiments. For liquid and amorphous materials, diffraction experiments yield only a one-dimensional projection of the real three-dimensional structure in the form of a pair-correlation function. Information on three- and many-body correlations from other types of experiments (e.g., extended x-ray-absorption fine-structure, x-ray-absorption near-edge structure, etc.) is rather uncertain and incomplete.[2] Therefore, to explore the structure of amorphous materials in sufficient detail, the laboratory experiment must be supplemented with a computer experiment. One may distinguish three different strategies for the computer modeling of amorphous structures: (a) accretion, i.e., the sequential addition of atoms to a growing cluster;[3] (b) randomization and relaxation: a highly random structure is created by disordering a regular structure (for amorphous Si or Ge, for example, one starts from a diamond structure and introduces disorder by switching nearest-neighbor bonds) and relaxing towards a low-energy structure which is still random;[4] (c) molecular dynamics. Processes (a) and (b) produce results that are strongly biased by the details of the growth, respectively, randomization algorithm and by the interatomic force field used in the relaxation. Molecular dynamics is recommendable since the results depend only on the quality of the interatomic potentials. Indeed molecular dynamics has been applied with much success to the simulation of liquid and amorphous metals[5] and salts,[6] based on potentials that are essentially parameter free and derived from first principles.[7]

The more difficult case is that of the semiconducting elements and compounds, especially of those materials that are semiconducting and fourfold coordinated in the solid (crystalline or amorphous) phase,[8–10] but metallic with a higher coordination number ($N_c \geq 6$) in the liquid state.[11–13] This is the case for the semiconducting elements Si and Ge and for the III-V compounds like Ga-As. Classical molecular dynamics simulations based on effective pair and volume forces derived from pseudopotential- and linear-response theories[7] describe the liquid structure of Si, Ge, and GaAs remarkably well,[14–16] but a simulated quench using these potentials leads to an overcoordinated amorphous material ($N_c \sim 5$) that is still metallic.[14] The reason is that the linear response of the electron gas is unable to describe the profound modification of the interatomic forces that accompanies the liquid-metal to amorphous-semiconductor transition. Since quantum-mechanical techniques for calculating three- and many-body forces in covalently bonded materials are still in their infancy,[17] large efforts have been directed towards the construction of empirical two- and three-body potentials[18–20] for Si and Ge, supported by a large basis of data from experiment and *ab initio* calculations. The application to the simulation of liquid and amorphous phases shows that the transferability of these potentials is limited: for the liquid phase, the influence of tetrahedral bonding is overestimated,[18,21] but nonetheless the recovery of a nearly perfectly fourfold-coordinated structure on cooling appears to be very difficult. A realistic description of the amorphous fourfold-coordinated network is achieved only if the strength of the three-body forces is artificially enhanced during cooling.[21–24] If this is not done, extremely low quenching rates are required,[22] in spite of the fact

that the local tetrahedral order is overestimated in the liquid. Again, these difficulties reflect the configuration dependence of the interatomic forces.

Hence the challenge is to calculate the full set of quantum mechanical many-body forces for each instantaneous atomic configuration of the system. This is now possible using the *ab initio* molecular dynamics (MD) techniques pioneered by Car and Parrinello.[25] The aim of the *ab initio* MD approach is to perform a simulation in which the interatomic forces are derived directly from the electronic ground state [calculated within density functional theory[26] (DFT)] using the Hellmann-Feynman theorem. In other words, for a given atomic configuration $\mathbf{R}_I$ the Born-Oppenheimer (BO) potential energy surface $E_{\mathrm{BO}}[\mathbf{R}_I]$ is obtained by minimizing the total-energy functional $E[\mathbf{R}_I, \psi_i]$ with respect to the one-electron states ψ_i. The force acting on an atom at the site $\mathbf{R}_I$ is then given as the derivative of $E_{\mathrm{BO}}[\mathbf{R}_I]$ with respect to $\mathbf{R}_I$. In the original Car-Parrinello (CP) method, instead of minimizing the total energy at any step of the simulation, the simultaneous time evolution of both the ionic and the electronic degrees of freedom is determined by integrating the following coupled equations of motion[25]

$$M_I \ddot{\mathbf{R}}_I(t) = -\frac{\partial E}{\partial \mathbf{R}_I(t)} \tag{1}$$

$$\mu \ddot{\psi}_i(\mathbf{r},t) = -\frac{\delta E}{\delta \psi_i^*(\mathbf{r},t)} + \sum_j \Lambda_{ij}\psi_j(\mathbf{r},t)\,. \tag{2}$$

Equation (1) is just the usual Newtonian equation of motion (EOM) for the ions with the forces calculated according to the Hellmann-Feynman theorem and Eq. (2) (where the Λ_{ij} are Lagrange multipliers for the orthonormality constraints to the wave functions and μ is a fictitious mass for the electronic degrees of freedom) is a pseudo-Newtonian equation of motion for the electronic degrees of freedom. The integration of the coupled EOM is started after the electronic wave functions have been relaxed to their ground state. The CP equations have been applied quite successfully to a number of systems, including the liquid[27] and amorphous[28,29] forms of Si.

Since the electronic wave functions of DFT are meaningful only if the electrons are in their ground state for the given ionic configuration, an essential condition for the practicability of the CP method is that the transfer of energy between the ionic and electronic subsystems is small to prevent the electron state from drifting away from the adiabatic or BO surface. In insulators or semiconductors, the width of the electronic band gap divided by the fictitious mass μ of the electronic degrees of freedom defines the separation of the characteristic frequencies of the ionic and electronic motions. In metals this separation is absent and the essential mechanisms that drives metallic systems into nonadiabaticity is level crossing between occupied and empty electron states.[30] The operational solution for this nonadiabaticity problem is (a) performing periodic energy minimizations to "bring the system back to the BO surface"[27] or (b) attaching the electronic subsystem to a Nosé thermostat[31] that prevents the heating up of the electron system. Since both the periodic energy minimizations and the thermalization of the electron states break the microcanonical evolution of the coupled electron-ion system, control of the temperature of the ions is possible only if the ions are coupled to a second Nosé thermostat. This is equivalent to inclusion of additional forces in Eqs. (1) and (2) which describe the coupling to two external heat baths serving to keep the average ionic temperature constant and equal to a prescribed value T and to limit the distance of the electrons from the BO surface.[32] It is clear that the nonadiabaticity problems are relevant to the simulation of liquid-metal–amorphous-semiconductor transition. In the work of Stich *et al.* on liquid and amorphous Si the nonadiabaticity problem was handled by using a canonical ensemble (with the ionic Nosé thermostat), periodic electronic energy minimizations, and a large electronic mass parameter μ in the liquid state and during the quench and annealing phases, and a microcanonical ensemble, free evolution of the electron states and a small value of μ during equilibration in the amorphous state.[29] Empty electron states were ignored.

The alternative is to perform the minimization of the DFT functional for the electronic energy at any time step of the MD simulation, so that the problem of nonadiabaticity does not arise at all. For the level-crossing problem, it is clear that instabilities in the evolution of the electron states can be avoided by allowing for variable fractional occupation numbers. Fractional occupancy of electron states appears very naturally in the finite-temperature version of DFT.[33]

In the present paper we report *ab initio* MD simulations of the liquid and amorphous phases of Ge based on (a) finite-temperature density-functional theory, (b) energy minimization after each MD step using a efficient iterative matrix-diagonalization scheme based on conjugate-gradient methods, (c) accurate nonlocal pseudopotentials evaluated in real space, and (d) a canonical ensemble in the Nosé formulation. In Sec. II we outline the basic ingredients of our technique and demonstrate that even from the point of view of computational efficiency, the method is at least comparable to the CP algorithm. Details of the simulation of the liquid phase and of the preparation of an amorphous sample using a simulated quench, as well of the subsequent annealing treatment are given in Sec. III. The structural and electronic properties of the liquid, supercooled liquid, and amorphous phases are discussed in Sec. IV, including a detailed comparison with experiment. Some preliminary results on liquid Ge have been published recently in two short communications.[34,35] The dynamical properties are described in Sec. V. Section VI analyzes the characteristic coordination and spectral defects in the quenched and annealed amorphous sample.

The main results of our study are as follows.

(a) We demonstrate the feasibility of fully dynamical simulations for liquid metals and of the simulation of quench condensation using *ab initio* MD techniques based on direct energy minimization. (b) Structural, dynamic, and electronic properties of the liquid and amorphous phases are in very good agreement with experiment. (c) Contrary to simulations using empirical many-

body forces,[21–23] the use of accurate quantum many-body forces allows us to prepare a realistic model structure for the amorphous semiconductor using a very rapid quench.

II. THEORY: *ab initio* MD USING DIRECT ENERGY MINIMIZATION

Our *ab initio* MD routine is based on the following principles.

(1) We use the finite-temperature version of the DFT developed by Mermin.[33] Exchange correlation is described by the local-density functional of Ceperley and Alder.[36] At finite temperature the free energy $F[n(\mathbf{r}), f_i, \mu]$ depending on the electron density $n(\mathbf{r})$, the Fermi-Dirac occupation probability f_i of the one-electron states $\psi_i(\mathbf{r})$ $[n(\mathbf{r}) = \sum_i f_i |\psi_i(\mathbf{r})|^2]$ and the chemical potential μ is the proper variational functional. The ground state may be found by minimizing $F[n(\mathbf{r}), f_i, \mu]$ with respect to $n(\mathbf{r}), f_i$ and μ. It has been shown that even at finite temperature, the proper DFT force is equal to the Hellmann-Feynman force.[37,38] Instead of the Fermi-Dirac broadening of the one-electron energies it may be computationally convenient to use a Gaussian broadening instead (see below).

(2) The minimization of the total energy (respectively, the total free energy) is performed using an efficient matrix diagonalization scheme based on a variant of the conjugate-gradient techniques developed by Payne and co-workers[39–42] and used in self-consistent electronic structure calculations by Bylander, Kleinman, and Lee.[43] The method is a doubly iterative one: in the inner loop the wave functions and eigenvalues for each $\mathbf{k}$ point in the Brillouin zone and for each band are improved for a *fixed* potential $V(\mathbf{r})$ by a preconditioned conjugate-gradient method[43] until the change in the eigenvalue has dropped below a fixed threshold, i.e., the conjugate-gradient method is used as a tool for iterative calculation of the lowest eigenvalues ($\leq 10\%$ of all eigenvalues) of the large Hamilton matrix. After running over all bands (including some empty bands), a subspace diagonalization is performed, the Fermi energy and new partial occupancies are calculated, and the charge density $n(\mathbf{r})$ and the potential $V(\mathbf{r})$ are updated.

(3) The atomic motion is described using Nosé dynamics generating a canonical ensemble.

(4) After moving the atoms, the new wave functions are estimated using the subspace alignment scheme proposed by Arias *et al.*[41]

(5) The calculation has been performed using an optimized nonlocal pseudopotential[44,45] in Kleinman-Bylander factorization using the real-space projection scheme.[40]

A. Finite-temperature density-functional theory

At finite temperature, the proper variational functional is the free energy of the electrons, subject to the constraints of the orthonormality of the wave functions and of a constant number $N_{\rm el}$ of electrons, i.e. (for simplicity we restrict the formulation to a single $\mathbf{k}$ point)

$$F[\psi_i(\mathbf{r}), f_i, \Lambda_{ij}, \mu] = E[\psi_i(\mathbf{r}), f_i] - \sigma S_{\rm el}[f_i] + \mu\Big(\sum_i f_i - N_{\rm el}\Big) + \sum_{i,j} \Lambda_{ij} \left(\int \psi_i^*(\mathbf{r}, t)\psi_j(\mathbf{r}, t)\, d^3\mathbf{r} - \delta_{ij} \right), \qquad \sigma = k_{\rm B} T_{\rm el} \quad (3)$$

where the first two terms contain the internal energy $E[\psi_i(\mathbf{r}), f_i]$ and entropy $S[f_i]$ of the electrons and the third and fourth terms express the constraints with the Lagrange-multiplicators Λ_{ij} and μ. In the ground state, the variation of $F[\psi_i(\mathbf{r}), f_i, \Lambda_{ij}, \mu]$ with respect to all four parameters must vanish: For nondegenerate states the matrix of Lagrange multipliers Λ_{ij} must be diagonal $\Lambda_{ij} = \delta_{ij}\epsilon_i$, and variation with respect to the wave functions ψ_i leads to the Kohn-Sham DFT eigenvalue equation

$$H|\psi_i\rangle = (T + V^{\rm sc})|\psi_i\rangle = \epsilon_i |\psi_i\rangle, \quad (4)$$

with the self-consistent one-electron potential $V^{\rm sc}$. Minimization with respect to f_i determines the relation to be satisfied by the fractional occupation numbers f_i,

$$\frac{dS_{\rm el}[f_i]}{df_i} = \frac{\epsilon_i - \mu}{\sigma}. \quad (5)$$

The entropy in Eq. (3) corresponds to noninteracting fermions,

$$S_{\rm el}[f_i] = -\sum_i \Big(f_i \ln f_i + (1 - f_i)\ln(1 - f_i) \Big) \quad (6)$$

with a Fermi-Dirac occupation probability of the one-electron states,

$$f_i = \left[\exp\left(\frac{\epsilon_i - \mu}{\sigma} \right) + 1 \right]^{-1}. \quad (7)$$

The property of being stationary with respect to f_i makes the gradient of the free energy F equal to the Hellmann-Feynman forces,

$$\mathbf{F}_I = -\frac{dF}{d\mathbf{R}_I} = -\sum_i f_i \left\langle \psi_i \left| \frac{\partial H(V^{\rm sc}, \mathbf{R}_I)}{\partial \mathbf{R}_I} \right| \psi_i \right\rangle \quad (8)$$

since the additional terms in the gradient of F depending on the variation of the occupation numbers and of the entropy term with the atomic displacement cancel exactly.[37,38]

To obtain a smooth variation of the f_i it is necessary to use an electron temperature that is significantly higher than the ionic temperature (depending on the level spacing and hence on the size of the system). In most cases we found it more convenient to use Gaussian broadening of the one-electron levels: it allows us to achieve a smooth variation of the occupation numbers around the Fermi level, but for higher excitation energies the occupation numbers converge more rapidly to zero. This improved

convergence allows one to reduce the necessary number of bands and hence the computational effort. The form of the entropy related to the Gaussian broadening is[46]

$$S = \frac{1}{2\sqrt{\pi}} \exp\left[-\left(\frac{\epsilon-\mu}{\sigma}\right)^2\right] , \tag{9}$$

where the occupation function f_i and the eigenvalues ϵ_i are related through

$$f_i = \frac{1}{2}\left(1 - \mathrm{erf}\left[\frac{\epsilon_i-\mu}{\sigma}\right]\right) \tag{10}$$

with σ equal to the width of the Gaussians.

B. Iterative matrix diagonalization based on conjugate-gradient minimization

Methods for determining the DFT-ground state via direct energy minimization have been developed by several groups.[39,42,43,47,48] We closely follow Bylander *et al.*[43] in using the conjugate-gradient method for improving the expectation value of the Hamiltonian

$$\langle\psi_i|H|\psi_i\rangle / \langle\psi_i|\psi_i\rangle \tag{11}$$

for all bands sequentially and then diagonalizing the Hamiltonian in the subspace of the improved eigenfunctions to obtain the starting states for the next iteration which begins after the potential has been updated.

The simplest strategy for minimization is the steepest descent approach, i.e., to change the approximate wave function ψ_i in the direction of the gradient g_i in the Hilbert space of the basis functions (plane waves in our case) from which ψ_i is constructed. If the Hamiltonian is diagonal in the subspace spanned by the trial wave functions, i.e.,

$$\langle\psi_i|H|\psi_j\rangle = \delta_{ij}\epsilon_i \tag{12}$$

the gradient is simply

$$g_i = (H - \epsilon_i)\,\psi_i \,. \tag{13}$$

The steepest-descent approach may be improved in two ways. (a) The conjugate gradient approach[39] changes the search direction from the direction of the steepest descent to one which points more nearly to the minimum by retaining information from previous search steps. (b) Preconditioning of the steepest descent accounts for the fact that due to the presence of the kinetic energy operator in H plane waves with the largest momentum will have the largest coefficients in g_i. Preconditioning[42] involves multiplying the coefficient of each plane wave in g_i by a factor which is close to unity for plane waves whose kinetic energy does not exceed the average kinetic energy of g_i and decreases strongly for the higher plane-wave components. In our work we used the preconditioning functions of Ref. 39. After the preconditioning a reorthogonalization of the conditioned gradient to all bands is necessary.

The iterative improvement of a state is stopped after the change in the energy eigenvalue is smaller than 10^{-6} eV (or less than 30% of the change in the first steepest-descent step) and the calculation moves to the next band. After running over all bands (including some empty bands) the Hamiltonian matrix

$$\langle\psi_j\,|H|\psi_i\rangle = H_{ij} \tag{14}$$

is diagonalized in the subspace spanned by the improved trial wave functions and the new Fermi energy and new occupation numbers are determined using Gaussian broadening. Using the new occupation numbers charge density and potential are updated. To prevent charge sloshing, the mixing scheme of Kerker[49] has been used:

$$n_{\mathrm{in}}^{N+1}(\mathbf{G}) = n_{\mathrm{in}}^{N}(\mathbf{G}) + A\frac{G^2}{G^2+G_0^2}\left[n_{\mathrm{out}}^{N}(\mathbf{G}) - n_{\mathrm{in}}^{N}(\mathbf{G})\right] ; \tag{15}$$

for our calculations of liquid and amorphous germanium we found fast convergence for $A = 1.0$, $G_0 = 1.5$ Å^{-1}. The electronic energy minimization is terminated after the change in the total energy per atom becomes smaller than 1×10^{-5} eV/atom. Our approach differs from the band-by-band conjugate-gradient minimization used by Teter *et al.*[39] In their approach the preconditioned conjugate-gradient method is used to minimize the *total energy*; charge density and potential are recalculated after each update of a band. For insulators and semiconductors where the occupation numbers do not change, this is a stable procedure. For metals the subspace diagonalization necessary for the calculation of the new occupation numbers leads to strong charge sloshing and the procedure might be unstable.

C. Nosé dynamics

The Nosé thermostat is a method for simulating a canonical ensemble at a prefixed temperature. The dynamics of the ions is described by the EOM

$$M_I\ddot{\mathbf{R}}_I(t) = -\frac{\partial E}{\partial \mathbf{R}_I(t)} - M_I\,\dot{\mathbf{R}}_I(t)\,\frac{\dot{s}(t)}{s(t)} , \tag{16}$$

where $s(t)$ is an additional variable that obeys the EOM

$$Q\frac{d(s(t)^{-1}\dot{s}(t))}{dt} = \sum_I M_I|\dot{\mathbf{R}}_I(t)|^2 - gk_BT \tag{17}$$

and describes the coupling of the physical system to a heat bath. Here Q is a mass parameter for the Nosé thermostat and $g = 3(N-1)$ counts the number of ionic degrees of freedom. The parameter Q determines the response of the heat bath to fluctuations of the ionic system. Q must be sufficiently small to allow the system to approach equilibrium fast enough, and sufficiently large to yield correct values for the energy fluctuations of the ionic system.[50] According to Nosé,[51] the characteristic frequency of the thermostat is

$$\omega_T^2 = \frac{2gk_BT}{Q} . \tag{18}$$

Equilibration between ions and thermostat is most effective if ω_T is of the same order of magnitude as the characteristic vibrational frequencies of the system since this leads to a strong coupling of both subsystems. In the present work we chose Q so that the period of the thermostat is equal to about 150 time steps ($\omega_T = 13.6\ \mathrm{ps}^{-1}$), we found very good agreement between Eq. (18) and the actual frequency of the temperature fluctuations.

The ionic equations of motion are integrated using a fourth-order predictor-corrector algorithm[52,14] which allows the use of time steps as large as $\Delta t = 3 \times 10^{-15}$ s with good energy conservation (note that this time step is about a factor of 10 larger than the time step in comparable CP simulations[27]).

In a microcanonical ensemble, the conserved quantity in a finite-temperature DF-MD is the sum of the kinetic energy T_I of the ions, of the internal energy E of the electron-ion system, and of the electronic entropy term $-TS_{\mathrm{el}}$,

$$\Omega_{\mathrm{mc}} = T_I + E\left[\mathbf{R}_I, \psi_i, f_i\right] - TS_{\mathrm{el}}[f_i] \ . \tag{19}$$

In the Nosé approach, the total energy of the electron-ion system is allowed to fluctuate, the conserved quantity is the expectation value of the extended system (ions + electrons + thermostat), i.e.,

$$\Omega = T_I + E[\mathbf{R}_I, \psi_i, f_i] - TS_{\mathrm{el}}[f_i] \tag{20}$$

$$+ \frac{1}{2}Q\left(\frac{\dot{s}}{s}\right)^2 + gk_BT\ln s \ . \tag{21}$$

Here the terms in the second line stand for the kinetic and potential energies of the extra degree of freedom s.

To speed up the calculations, the simulation of the liquid phase was started in the classical molecular dynamics mode with interatomic pair forces calculated using pseudopotential perturbation theory and an empty core pseudopotential (EC-PP) ($R_c = 1.03$ a.u.).[7,14] For the liquid metal Ge, this leads to a rather accurate description of the atomic and electronic structure.[14,15,35] After switching to the *ab initio* MD, the system reaches equilibrium within a small number of MD steps (less than 0.5 ps). This combination of classical and *ab initio* MD leads to an appreciable economy in computer time.

D. Subspace alignment

The initial wave functions for the starting configuration are generated by diagonalizing the Hamiltonian corresponding to a charge density of overlapping atoms in a basis of 200 plane waves.

After moving the ions, one needs a reasonable estimate of the electronic wave functions and the charge density n_{in} for the new configuration—the wave functions of the old configuration would give a bad starting point for the energy minimization. The charge density may be estimated by extrapolating the charge density calculated at times $t_n, t_{n-1}, \ldots$ to t_{n+1}, i.e.,

$$n(t_{n+1}) = n(t_n) + [n(t_n) - n(t_{n-1})] \tag{22}$$

to lowest order, and similarly for higher-order extrapolations. A corresponding extrapolation may be performed for the wave functions. However, one has to consider that as a consequence of the subspace diagonalization the wave functions are rotated in Hilbert space. Arias *et al.*[41] propose to transform the two sets of wave functions such that their distance D,

$$D = \sum_i w_i \left\|\psi_i'(t') - \psi_i'(t)\right\| \tag{23}$$

is minimal (w_i is some weighting function), and where

$$\psi'(t') = U'\psi(t'), \quad \psi'(t) = U\psi(t) \tag{24}$$

are the transformed wave functions, U, U' are unitary matrices. After performing both transformations, the overlap of the two sets of wave functions is

$$\langle\psi_j'(t')|\psi_i'(t)\rangle = \delta_{ij}\cos\Theta_i \ , \tag{25}$$

i.e., both subspaces are perfectly aligned. To first order, the extrapolation of the wave functions is trivial:

$$\psi(t_{n+1}) = 2U_n\psi(t_n) - U_n'\psi(t_{n-1}) \ . \tag{26}$$

Here U_n and U_n' are the unitary transformations that align the subspaces spanned by the wave functions at times t_n and t_{n-1}. Extensions to higher-order extrapolations are discussed in Ref. 53.

In simulations for metallic systems, empty states have to be considered. This helps to predict wave functions close to the Fermi energy because the wave functions at time t_{n+1} are to first order a linear combination of wave functions at t_n

$$|\psi_i(t_{n+1})\rangle = \sum_j \frac{\langle\psi_j(t_n)|[H(t_{n+1}) - H(t_n)]|\psi_i(t_n)\rangle}{\epsilon_i - \epsilon_j} \times|\psi_j(t_n)\rangle \ , \tag{27}$$

i.e., predominantly wave functions out of a small interval around ϵ_i are mixed. Our results show that even for liquid Ge the prediction of the wave functions leads to a state whose energy does not differ from the ground state energy by more than 5×10^{-5} eV/atom. On this basis, the relaxation to the ground state is usually possible within two conjugate-gradient iterations each requiring two evaluations of the Hamiltonian acting onto all wave functions.

For an ensemble of 64 Ge atoms, in the metallic liquid phase at $T \simeq 1250$ K, the change of the conserved energy Ω [see Eq. (16)] was smaller than 5 meV per atom over a run of 3 ps [i.e., $\sim$ 1000 steps with $\Delta t = 3 \times 10^{-15}$ s, see Fig. 1(a)]. This corresponds to less than 0.1% of the cohesive energy. For amorphous Ge at $T \sim 300$ K, the change in the total energy is smaller than 1 meV/Atom over a run of 6 ps [see Fig. 1(b)].

E. Nonlocal pseudopotentials in real-space projection

In our calculations we used a nonlocal Vanderbilt[44] pseudopotential with a cutoff radius of $R_c = 1.5$ a.u.,

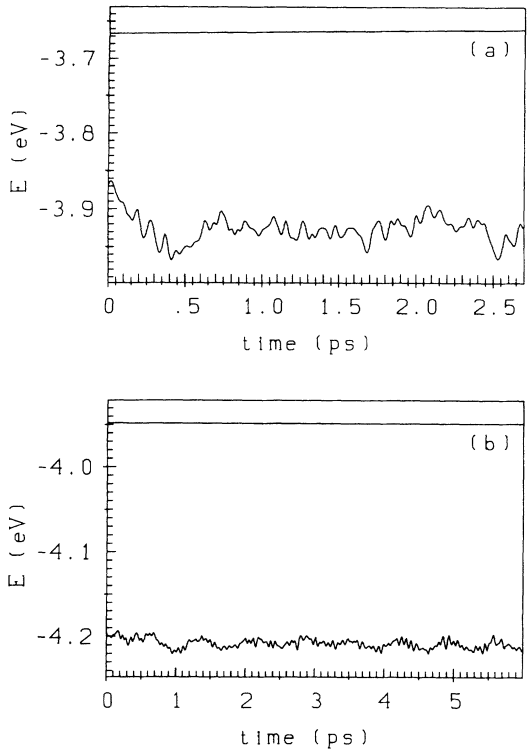

FIG. 1. Time evolution of the canonical constant of motion Ω [see Eq. (16), upper curve] and of the potential energy E (lower curve) under isothermal conditions in the liquid phase at $T = 1250$ K (a) and in the amorphous phase at $T = 300$ K (b).

generated from a scalar-relativistic all-electron calculation. The choice of the pseudopotential is the result of an extensive study of the optimization of the accuracy and plane-wave convergence of various norm-conserving pseudopotentials (NCPP) (Refs. 44, 45, and 54–56). This potential offers a compromise between computational efficiency, accuracy, transferability, and plane wave convergence. Energy cutoffs of 12 Ry and 25 Ry are necessary to converge the total energy of germanium to within 1 mRy and 0.1 mRy, respectively. The cutoff energy cannot be lowered substantially by, e.g., optimization of the kinetic energy.[56]

With this pseudopotential we calculate the lattice constant of Ge at $T = 0$ K in the diamond structure within 1.3% (see Table I) of the experimental value and a reasonable pressure for the $\alpha \rightarrow \beta$ (diamond structure $\rightarrow$ white-tin structure) transition ($P_c = 75$ kbar, expt. $P_c = 100$ kbar), see Fig. 2. Lattice constant, bulk modulus, and cohesive energy are in very good agreement with recent NCPP calculations of Garcia *et al.*,[57] the agreement with older calculations of Yin and Cohen[58] is worse, probably due to insufficient number of plane waves and due to the use of the Wigner exchange-correlation functional[59] in Ref. 58.

The Vanderbilt pseudopotential is nonlocal, we used a Kleinman-Bylander[60] factorization decomposing the nonlocal potential into a sum of diagonal operators for the individual angular momentum components,

TABLE I. Lattice constant a_0, equilibrium volume V_0, bulk modulus B_0, and cohesive energy E_c for cubic diamond Ge (spin correction for atoms were included in the present calculation).

	PP[a]	Garcia *et al.*[b]	Yin *et al.*[c]	Experiment
E_c (eV)	4.55	4.79	4.26	3.85
V_0 (Å^3)	21.61	21.36	22.60	22.64
a_0 (Å)	5.57	5.55	5.66	5.66
B_0 (Mbar)	75	78	73	76.8

[a]Present work, Ceperley-Alder exchange-correlation functional.
[b]Reference 57, Ceperley-Alder exchange-correlation functional.
[c]Reference 58, Wigner interpolation for exchange-correlation functional.

$$V = V_{\rm loc} + \sum_{\ell m} \frac{|\Phi^{\rm ps}_{\ell m}\Delta V_\ell\rangle\langle\Delta V_\ell \Phi^{\rm ps}_{\ell m}|}{\langle\Phi^{\rm ps}_{\ell m}|\Delta V_\ell|\Phi^{\rm ps}_{\ell m}\rangle}\ , \tag{28}$$

where the $\Phi^{\rm ps}_{\ell m}$ are the pseudoatom wave functions and $\Delta V_\ell = V_\ell - V_{\rm loc}$ is the nonlocal part of the pseudopotential. For Ge we chose the p component as the local component and considered s and d nonlocality.

The nonlocality of the pseudopotentials extends only over the region occupied by the core of the atom. Hence it is possible to deal efficiently with the nonlocality of the potential by working in real space. For this specific pseudopotential we found that optimization of the real-space projection operators (see King-Smith *et al.*[40]) is not necessary, because the Fourier components of the projection states $\Phi^{\rm ps}_{\ell m}\Delta V_\ell$ decay rather rapidly to zero.

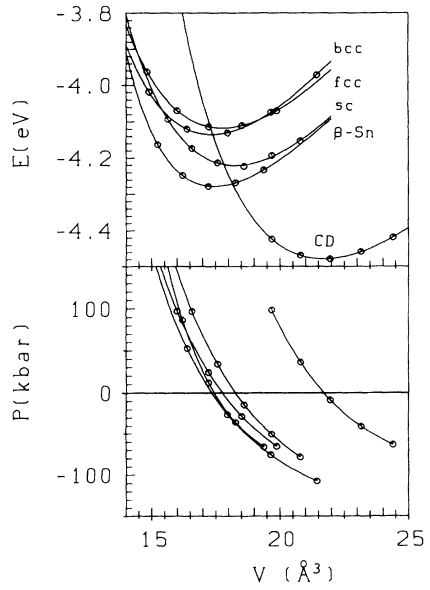

FIG. 2. Energy E and pressure P vs volume V for solid Ge in different crystal structures, calculated with the pseudopotential used in the *ab initio* MD simulation: cubic diamond (CD), β-Sn, face-centered cubic (fcc), body-centered cubic (bcc) and simple cubic (sc).

III. SIMULATION OF THE LIQUID METAL–AMORPHOUS-SEMICONDUCTOR TRANSITION

Our simulations for liquid and amorphous Ge have been performed for an ensemble of 64 atoms in a cubic cell. For this ensemble, we calculated the wave functions for 138 bands, i.e., 10 bands more than necessary to accommodate the 256 valence electrons. A Gaussian broadening of the one-electron energies with $\sigma = 0.2$ eV was used. The wave functions at the Γ point were expanded in a basis of 7000 plane waves with a cutoff energy of 12 Ry. For the real- and reciprocal-space representation of the charge density and potential a $32 \times 32 \times 32$ mesh was used.

The simulation was started in the liquid phase at a temperature of $T = 1250$ K and a density of $n = 0.04385$ Å^{-3}. A starting configuration for the *ab initio* MD was generated by classical MD using effective pair potentials generated via second-order perturbation theory and an empty core pseudopotential with $R_c = 1.03$ a.u. If a pseudopotential optimized for the convergence of the perturbation series is used,[45] the classical simulation already leads to very accurate pair correlation functions[14–16,35] (for a detailed comparison of classical and quantum MD, see Ref. 35). After switching to the *ab initio* MD, the system converges very rapidly to the new ground state. Altogether we performed a 4.5 ps run (1500 time steps) at $T = 1250$ K (the thermal history of the ensemble is documented in Fig. 3 and Table II), averages are taken over 2.7 ps.

In the next step, the system was quenched at constant density from $T = 1250$ K to 750 K in 3 ps (1000 steps), i.e., at a quench rate of $\dot{T} = 1.67 \times 10^{14}$ K s^{-1}, from $T = 750$ K to $T = 450$ K in 4.5 ps (1500 steps, $\dot{T} = 0.67 \times 10^{14}$ K s^{-1}) and finally from $T = 450$ K to $T = 300$ K in 0.9 ps (300 steps, $\dot{T} = 1.67 \times 10^{14}$ K s^{-1}). Subsequently the system was equilibrated at $T = 300$ K for 200 steps, followed by a production run. The overall thermal treatment took 15 ps.

In previous MD runs we had noticed that the most important structural changes occur in the temperature range $750 - 450$ K. At higher temperatures the system is still in the metallic phase, hence the changes in the local geometry are small. At lower temperatures, the atomic mobility [as monitored by the mean-spare displacements, see (Fig. 4)] is very low. This is the rationale for quenching the system rather rapidly at higher and lower temperatures.

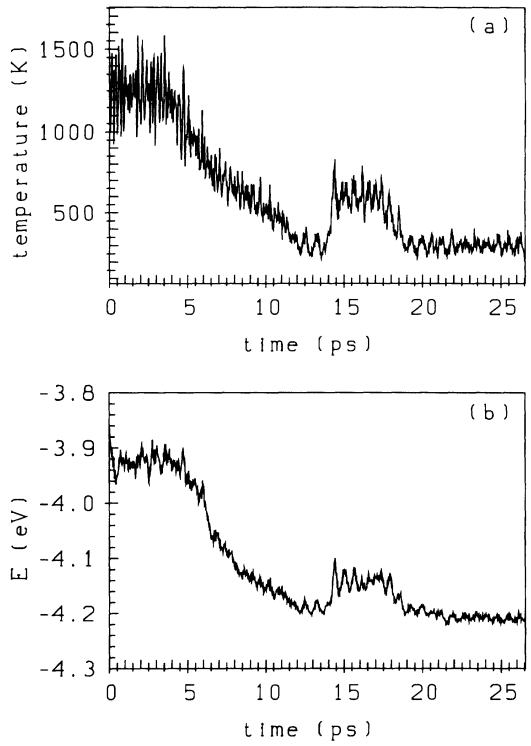

FIG. 3. Time evolution of the instantaneous temperature T (a) and of the potential energy (b) during the MD run.

Our assumption that the densities of liquid Ge at $T = 1250$ K and of amorphous Ge at $T = 300$ K are equal is admittedly somewhat arbitrary. It is equivalent to the assumption that the density of amorphous Ge is about 1% lower than the experimental equilibrium density of crystalline Ge. However, we have to remember that the local-density approximation (LDA) overestimates the density by about 4.5% (see the data for crystalline Ge in Table I). Hence our assumption for the density of amorphous Ge is equivalent to assuming a density deficit of nearly 6% (relative to the LDA-equilibrium density of α-Ge). Experimental estimates of the density of thin vapor-condensed amorphous films of Ge[8,61] claim density deficits of up to 10%; for electrolytic a-Ge a density deficit of 5 % has been found. Most continuous-random network models[3,4,62–65] predict a density change between

TABLE II. History of quench and annealing cycle.

	Time steps	T_{start}	T_{end}	$\dot{T}$ (K s^{-1})	
4.5 ps	1500	1250			liquid
3 ps	1000	1250	750	1.67×10^{14}	cooling
4.5 ps	1500	750	450	0.67×10^{14}	
0.9 ps	300	450	300	1.67×10^{14}	
2.1 ps	700	300			as-quenched amorphous
0.3 ps	100	300	600		heating
3.0 ps	1000	600			annealing
1.8 ps	600	600	300	1.67×10^{14}	cooling
7.5 ps	2500	300			annealed amorphous

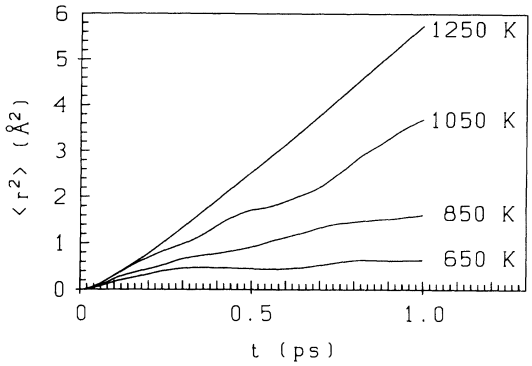

FIG. 4. Mean-square displacement $\langle r^2(t)\rangle$ of the Ge atoms at different temperatures in the liquid and undercooled liquid regime.

+1% and −4% with the exception of the Steinhardt[66] model predicting a decrease by −10%. It seems to be fair to conclude that the experimentally estimated density deficit arises to a large extent from microscopic voids at length scales outside the range of our model. In principle, the equilibrium atomic volume could be calculated in the *ab initio* MD simulation. However, this would result in a further increase of the already large computational effort. In our simulation we have verified that the internal pressure is small at the assumed atomic volume of the amorphous phase ($p = -4$ kbar at $T = 300$ K, after a correction of $p = -22$ kbar due to Pulay stress[67]).

The first quench results in a structure with a relative large number of geometrical defects. Therefore, we have made an attempt to improve the model by a simulated annealing: the temperature was first raised in about 0.3 ps to 600 K and the system was equilibrated at this temperature for about 3 ps. After a quench to $T = 300$ K, the system was reequilibrated for 4.5 ps (see Fig. 3 and Table II); a production run of 3.0 ps followed.

The analysis of the time evolution of local geometrical defects in the amorphous phase shows that even the small thermal fluctuations at room temperature can cause the generation and annihilation of local defects (see also the recent study of the finite-temperature properties of amorphous Si by Drabold *et al.*[68]). To investigate the inherent (i.e., temperature-independent) defects of a-Ge, we have performed a projection of an instantaneous room-temperature configuration on the nearest potential-energy minimum using a quasi-Newton quench (see, e.g., Ref. 69). It has been shown[70,71] that the projection on potential-energy minima emphasizes the characteristic features of liquid and amorphous structures. In addition to the slow quench from 600 K to 300 K we also performed one fast quench (0.3 ps) to 300 K. After equilibration for 3 ps a second $T = 0$ configuration was created using quasi-Newton relaxation to the instantaneous ionic ground state. The configuration we obtained from this quench was—probably by accident—energetically more stable ($\Delta E = 0.4$ eV) than the first $T = 0$ configuration.

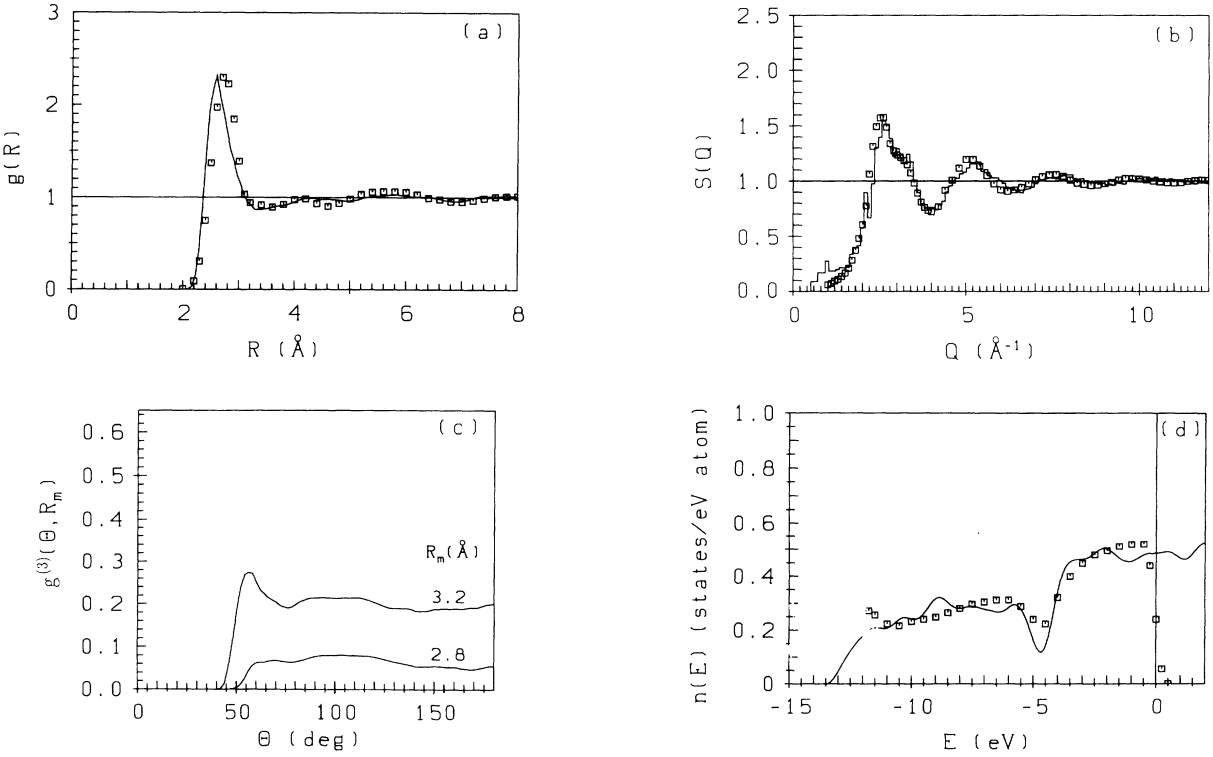

FIG. 5. Pair correlation function $g(R)$ (a), static structure factor S(Q) (b), bond-angle distribution function $g^{(3)}(\Theta, R_m)$ (c), and electronic density of states $n(E)$ (d) for liquid Ge at $T = 1250$ K. Full lines—*ab initio* MD; squares—experiment [neutron diffraction—Ref. 12 for $g(R)$ and $S(Q)$, photoemission—Ref. 75 for $n(E)$].

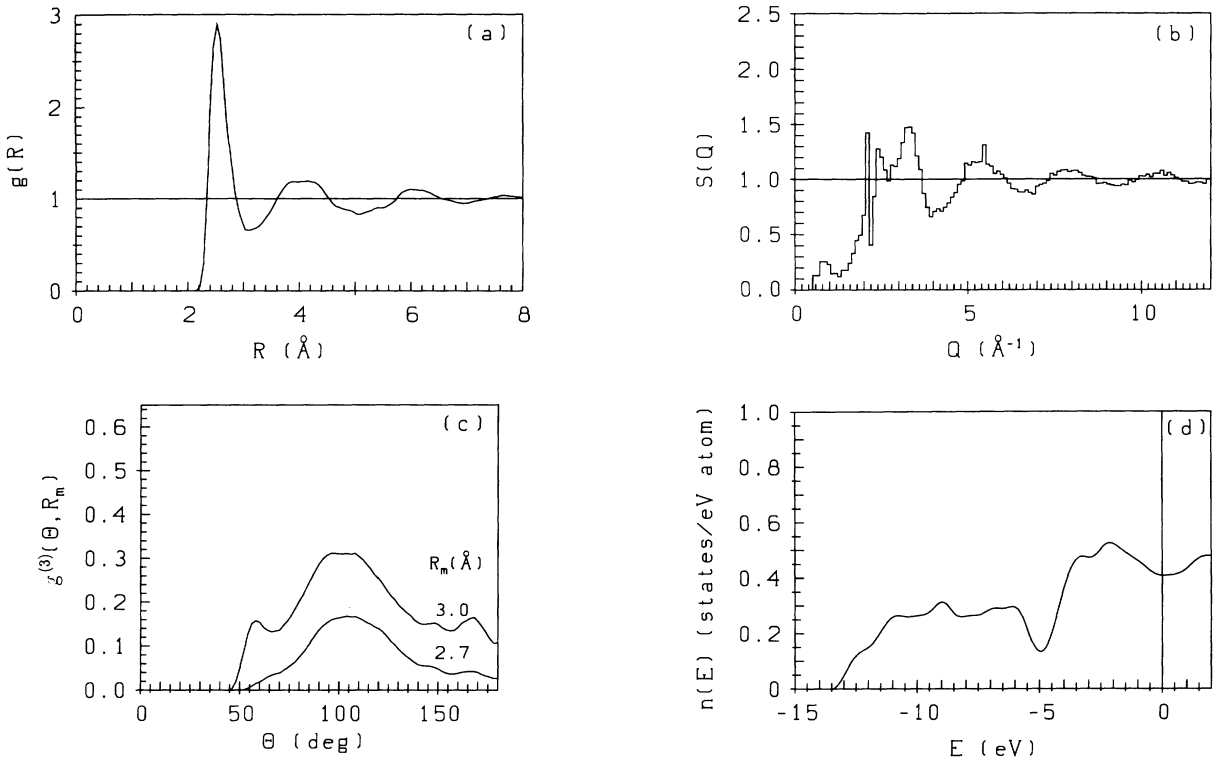

FIG. 6. Same as Fig. 5, but for supercooled liquid Ge in the temperature range 750 – 650 K.

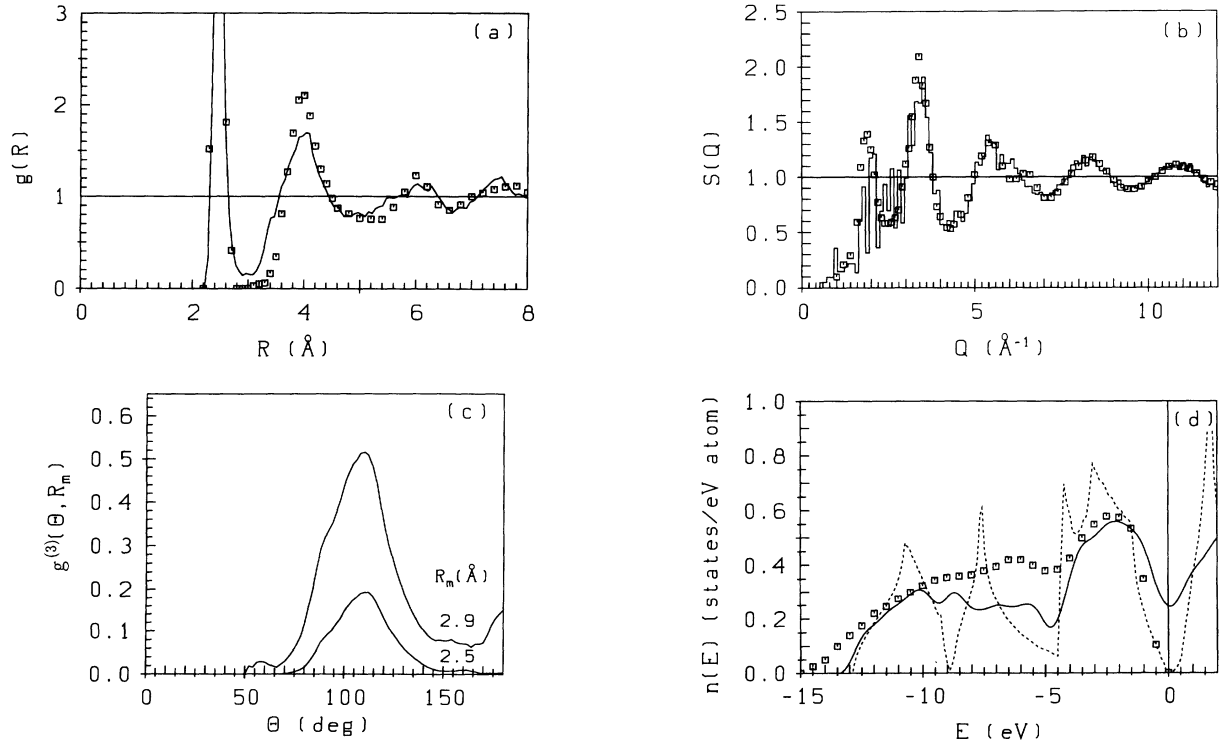

FIG. 7. Same as Fig. 5, but for as-quenched amorphous Ge at T = 300 K. The experimental data are from Ref. 8 [$g(R)$ and $S(Q)$, neutron diffraction] and Ref. 79 [$n(E)$, photoemission].

IV. ATOMIC AND ELECTRONIC STRUCTURE

In this section we discuss the atomic and electronic structure of our Ge sample in the liquid and amorphous states and the changes that occur during quenching and annealing. Figures 5–8 show the pair-correlation function $g(R)$, the static structure factor $S(Q)$, the bond-angle distribution function $g^{(3)}(\Theta, R_m)$ (i.e., the angles formed by nearest-neighbor bonds with a maximum length R_m around a central atom), and the electronic density of states $n(E)$ for liquid Ge at $T = 1250$ K, for a supercooled liquid Ge in the temperature range 750–650 K (the information has been sampled during a continuous cooling run), and for as-quenched and annealed amorphous Ge at $T = 300$ K. The static structure factor S(Q),

$$S(Q) = \left\langle \frac{1}{N} \sum_{\ell,m} e^{i\mathbf{Q}\cdot(\mathbf{R}_\ell - \mathbf{R}_m)} \right\rangle \tag{29}$$

has been calculated by performing in (29) the sum over all atom pairs for the **Q** vectors compatible with the periodic boundary conditions. Calculation of $S(Q)$ by Fourier transforming $g(R)$ can lead to results that are seriously affected by truncation errors. The electronic density of states (DOS) has been obtained by a Gaussian broadening ($\sigma = 0.4$ eV) of the 150 lowest eigenvalues at a $6 \times 6 \times 6$ Monkhorst-Pack grid[72] using one typical configuration. We found that a smooth and realistic DOS can be obtained using only the ten special points in the irreducible wedge of the simple cubic Brillouin zone generated from this state. The usual practice to consider the one-electron states at the Γ point only is sufficiently accurate for the calculation of the interatomic forces and pressure (this was tested by calculating the pair-correlation function and pressure for l-Ge using the off-symmetry **k** point $[(0.25, 0.25, 0.25)\pi/L]$ instead of the Γ point), but leads to spurious structures in the DOS that disappear after a more extended **k**-space sampling.

A. Liquid Ge

Our present simulation yields a very accurate description of the structure of liquid Ge. Figure 5 shows $g(R)$ and $S(Q)$ together with the experimental neutron diffraction data[12]—agreement between theory and experiment is indeed very good. The atomic arrangement in liquid Ge is very different from that in normal liquid metals. The coordination number N_c, obtained by integrating the radial distribution function $\mathrm{RDF}(R) = 4\pi R^2 n g(R)$ up to the first minimum at $R_m = 3.2$ Å(3.4 Å) is $N_c = 5.8$ (6.9), i.e., considerably lower than the value $N_c \sim 10 - 12$ characteristic for normal simple metals, but in good agreement with experiment[11] ($N_c = 6.8$), see also Table III. Besides the first peak, there are only weak oscillations in $g(R)$ that are well reproduced by the *ab initio* simulations. The characteristic feature of $S(Q)$ is the low amplitude of the main peak and the shoulder at $Q = 2k_F = 3.46$ Å^{-1} corresponding to the diameter of the free-electron Fermi sphere. The bond-angle distribution function $g^{(3)}(\Theta, R_m)$ is just the radial inte-

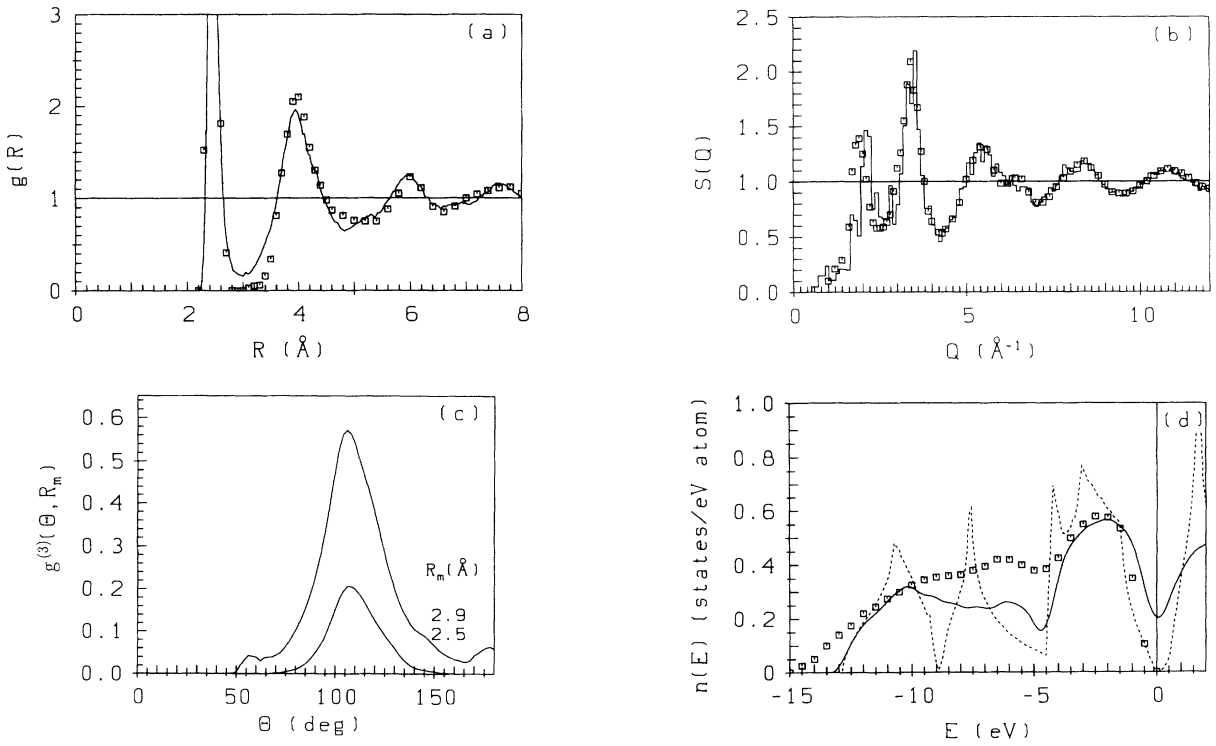

FIG. 8. Same is Fig. 5, but for annealed amorphous Ge at $T = 300$ K. The experimental data are the same as in Fig. 7. The dashed lines show for comparison the DOS of crystalline Ge (cf. text).

TABLE III. Average nearest-neighbor distance d_1, coordination number N_c, and bond angle Θ and their root-mean-square derivations in liquid and amorphous Ge (calculated at different maximal bond lengths R_m).

	R_m (Å)	d_1 (Å)	Δd_1 (Å)	N_c	Θ (deg)	$\Delta\Theta$ (deg)
l-Ge, T= 1250 K						
ab initio MD	3.2	2.75	0.24	5.8	99.4	31.7
ab initio MD	3.4	2.84	0.29	6.9	98.3	32.8
classical MD[a]	3.4	2.72		7.3	100.5	
exp.[b]		2.75		6.8		
sl-Ge, T = 750–650 K	3.0	2.63	0.17	4.63	103.1	26.8
a-Ge, T = 300 K, as-quenched	2.8	2.48	0.10	4.04	107.7	17.9
a-Ge, T = 300 K, annealed	2.8	2.49	0.10	4.05	107.7	16.9
a-Ge, T = 0 configuration 1	2.8	2.48	0.08	4.06	107.7	16.2
a-Ge, T = 0 configuration 2	2.8	2.46	0.06	3.97	108.5	14.9
Exp.[c]		2.463	0.047	3.68	108.5	
Exp.[d]		2.46	0.085	3.88	108.0	
CRN[e]		2.46		4	108.5	12.5
c-Ge		2.45		4	109.3	

[a]Calculated using effective pair forces based on EC-PP (R_c = 1.03 a.u.), see Ref. 14.
[b]Reference 11.
[c]Reference 8.
[d]Average over nine sets of experiments reviewed in Ref. 8.
[e]Wooten-Winer-Weaire continuous random-network model, Ref. 4.

gral over the triplet-correlation function $g^{(3)}(\Theta, R_1, R_2)$ for $R_1, R_2 < R_m$. Figure 5(c) shows that except for excluded-volume effects the distribution of the bond angles is almost random, with only a very flat maximum close to the tetrahedral bond angle of $\Theta = 109°$ for short bonds, and a preference for the formation of isosceles triplets ($\Theta \sim 60°$) for longer bonds. This corresponds to the very broad distribution of coordination numbers ranging from $N_c = 3$ to $N_c = 8$ (see Table IV).

The predictions of *ab initio* MD are very similar to those of classical MD with effective pair and volume forces calculated using pseudopotential and linear-response forces:[14–16,35] $g(R)$ and $S(Q)$ are almost identical, only at the level of the triplet-correlation functions we find that the quantum-mechanical many-body forces induce a slight preference of tetrahedral bond angles over close-packed configurations. In a similar way, the *ab initio* simulations of Stich *et al.*[27] have confirmed the pair-potential results for ℓ-Si.[15] This is important since it demonstrates that the real-space interpretation of the structures of *l*-Si and *l*-Ge in terms of a packing of soft spheres modulated by the Friedel oscillations in the interatomic forces (wavelength $\lambda_F = 2\pi/2k_F$) is correct.[14–16,73] In momentum space, the signature of the modulation of $g(R)$ is the shoulder in $S(Q)$ at $Q = 2k_F$.

For ℓ-Si, the calculated electronic DOS conforms with the nearly-free-electron (NFE) interpretation of the structure-force relationship: the calculated $n(E)$ is very close to a free-electron parabola.[27] The calculated DOS of liquid Ge shows a remarkable pseudogap at a binding energy of 4.5 eV. This makes the electronic DOS very different from any of the crystalline phases: it has neither the characteristic signature of the sp^3 hybridization of the semiconducting α and the metallic β phases, nor the free-electron character of the metallic high-pressure phases.[74] The calculated DOS is in very good agreement with high resolution photoemission data[75] and with earlier supercell-linear-muffin-tin-orbital (LMTO) calcula-

TABLE IV. Distribution of the number of nearest neighbors in liquid and amorphous Ge.

Percentage of nearest neighbors with N_c =	R_m (Å)	3	4	5	6	7	8
l-Ge, T = 1250K	3.2	1.2	11.2	29.3	31.4	19.7	7.2
sl-Ge, T = 750–650 K	3.0	4.8	43.5	37.4	14.3		
a-Ge, T = 300 K, as-quenched	2.8	4.9	86.8	7.8	0.5		
a-Ge, T = 300 K, annealed	2.8	4.6	85.0	10.3			
a-Ge, T = 0 configuration 1	2.8	4.7	84.4	10.9			
a-Ge, T = 0 configuration 2	2.8	6.3	90.6	3.1			

tions for the classical-MD models of ℓ-Ge.[15,74] The comparison with the LMTO calculations is helpful since these calculations show that the pseudogap in $n(E)$ separates s and p states (the lower part of the valence band accommodates exactly $2s$ electrons per Ge atom). The existence of the pseudogap is characteristic for the heavier liquid group IV elements (Ge,Sn,Pb), due to an increasing s-p splitting arising from realistic effects. In Ge the splitting is enhanced by a partial penetration of the $4s$ electrons in the $3d$ core leading to a stronger s component of the electron-ion pseudopotential.

In the past, various structural models for describing the short-range order ℓ-Si and ℓ-Ge have been proposed. They either assume the presence of two kinds of atoms (fourfold coordinated semiconducting or highly-coordinated metallic)[11,76] or assume a similarity with the β-Sn or simple cubic structures (both sixfold coordinated and metallic).[77] Our results for ℓ-Ge (as well as the results of Stich *et al.*[27] for ℓ-Si) indicate a broad, homogeneous distribution of local bonding configurations and indicate that both classes of models are unrealistic. The *ab initio* MD also demonstrates that for the liquid-metallic phase of Si and Ge, the effective pair and volume forces derived from pseudopotential perturbation theory[14–16] are much more realistic than the empirical pair and triplet forces[18–20] leading to unrealistic bond-angle distributions.

B. Supercooled liquid Ge

Continuous rapid quenching of ℓ-Ge from 1250 K (just above the melting point) to temperatures of $\sim$ 750 K leads to the formation of a metallic supercooled liquid: the first and second peaks in $g(R)$ grow in amplitude and become more symmetric (Fig. 6). The average coordination number decreases to $N_c = 4.63$ (Table III), the analysis of the local coordinations shows that higher coordinations ($N_c \geq 6$) with longer bonds are strongly reduced (Table IV). In the bond-angle distributions tetrahedral angles are now dominant, but there is still an appreciable number of close packed ($\Theta \sim 60°$) and a small number of collinear ($\Theta \leq 180°$) configurations [Fig. 6(c)]. In the static structure factor the peak close to $Q \sim 2k_F$ has the largest amplitude, the first peak has been damped and shifted to smaller momentum transfers. The only change in the electronic DOS is a slight decrease at the Fermi energy [Fig. 6(d)]. This state is clearly liquid and metallic, although the diffusion coefficient has decreased by a factor of $\sim$ 4 compared to the melting point (see also Fig. 4). This supercooled state is still rather well described by classical MD simulations with pseudopotential derived forces,[14] although the increase of the local tetrahedral order with decreasing temperature is certainly underestimated.

More pronounced structural changes occur only at temperatures below $T_a \sim 750$ K. Note that the reduced value of this "amorphization temperature" $T_a/T_m = 750/1250 = 0.6$ is about the same as for Si.[27] The persistence of fluidity and metallicity down to these relatively low temperatures is explained by the mechanism of the metal-semiconductor transformation: above T_m a small number bonds has a covalent character [$\sim$ 13%, counting the threefold- and fourfold-coordinated sites, or $\sim$ 25%, counting the nearest-neighbor bonds shorter than the covalent bond length of Ge ($2R_{\text{cov}} = 2.45$ Å) for which tetrahedral angles prevail]. These bonds are also characterized by a bond charge (i.e., a charge accumulation at midbond position in excess to a superposition of spherical free-atom charges). As the local configurations fluctuate at the time scale of the diffusive motion, the covalent bonds are rapidly destroyed and reformed. Only at a reduced atomic mobility covalent bonds that have once been formed survive and the metal-semiconductor transition occurs rather quickly. Experimentally the "glass transition" observed in laser-glazing experiments[78] is rather sharp. However, any significant observation of the character of the transition is prohibited by the large fluctuations in our small samples.

C. Amorphous Ge

Our results for the structural and electronic properties of as-quenched amorphous Ge are given in Fig. 7. The agreement of the calculated $g(R)$ and $S(Q)$ with the neutron-diffraction is good, the main difference is that the separation of the first two peaks in $g(R)$ [and to some extent also in $S(Q)$] is less pronounced in the computer experiment. The computer-generated amorphous sample is slightly overcoordinated ($N_c = 4.04$), indicating that fivefold coordinated defects are somewhat more frequent than threefold-coordinated sites (see Tables III and IV). The DOS in the gap at the Fermi level is strongly reduced, the overall shape of the DOS represents the photoemission intensities[79,80] rather well.

Annealing leads to a distinct improvement of the agreement between simulation and experiment (see Fig. 8), but no reduction of the number of defects. This concerns, in particular, the medium-range order as represented by the higher-order oscillations in $g(R)$. The model is still slightly overcoordinated ($N_c = 4.05$), fivefold defects dominate over threefold-coordinated sites. That some experiments give lower coordination numbers is almost entirely due to the underestimate of the microscopic density by nearly 10% (see above). The width of the bond-angle distribution ($\Delta\Theta \sim 17°$) is slightly larger than in the best continuous random network models adjusted to the experimental diffraction data (see Table III).

The calculated DOS at the Fermi level is reduced by annealing, the calculated $n(E)$ is in very good agreement with the photoemission data.[79,80] Compared to the liquid state, the pseudogap at $E_B \sim -4.5$ eV persists, a second gap develops at the Fermi level, a shallow DOS minimum appears at -7 eV. The three regions of the DOS below -7 eV, between -7 eV and -4.5 eV, and between -4.5 eV and the Fermi level correspond rather well to the three sp^3 subbands of the crystalline tetrahedral semiconductors (the S, M, and P parts of the valence band according to the conventional nomenclature[81]). This indicates an sp^3 hybridization of the valence band similar to the crystal and in contrast to the metallic liquid.

The DOS in the gap at the Fermi level remains finite, independently of the **k**-space sampling and the level broadening. An analysis of the charge distribution of the states in the gap shows that these states tend to be localized (see also Sec. VI).

V. ATOMIC DYNAMICS

The MD-generated trajectories allow us to investigate atomic transport and dynamics.

A. Single-particle dynamics and atomic transport

The simplest way to investigate atomic transport in liquids is to derive the self-diffusion coefficient D from the time dependence of the mean-square displacement[82]

$$\langle r^2(t)\rangle = \langle [\mathbf{R}_I(t) - \mathbf{R}_I(0)]^2 \rangle \tag{30}$$

$$= 6Dt + c \quad \text{for } t \to \infty \ , \tag{31}$$

where D is the self-diffusion coefficient and c is a constant. The average in (23) has to be taken over the ensemble and over different starting points along the trajectory. $\langle r^2(t)\rangle$ for various temperatures is shown in Fig. 4, the diffusion constant as a function of temperature is given Fig. 9. The value close to the melting point ($D = 1.0 \times 10^{-4}$ cm^2 s^{-1}) is of the same order of magnitude as for liquid Si near the melting point [$D = 2.0 \times 10^{-4}$ cm^2 s^{-1} (Ref. 47)]; no data for ℓ-Ge are available (but see *Note added in proof*). At the temperature where the metal-semiconductor transition is thought to begin, the diffusibility has dropped to about 6% of its value at the melting point.

An alternative access to the diffusion coefficient is via the velocity autocorrelation function $\psi(t)$ defined by[82]

$$\psi(t) = \frac{\langle \dot{\mathbf{R}}_I(t) \cdot \dot{\mathbf{R}}_I(0) \rangle}{\langle \dot{\mathbf{R}}_I(0) \cdot \dot{\mathbf{R}}_I(0) \rangle} \ . \tag{32}$$

Again, the average is over the ensemble and over different starting points along the equilibrium part of the MD trajectory. The diffusion coefficient D is then given by

$$D = \frac{k_B T}{M} \int_0^\infty \psi(t)\, dt \ . \tag{33}$$

The results are given in Fig. 9 and are in good agreement with the values derived from the mean-square displacements.

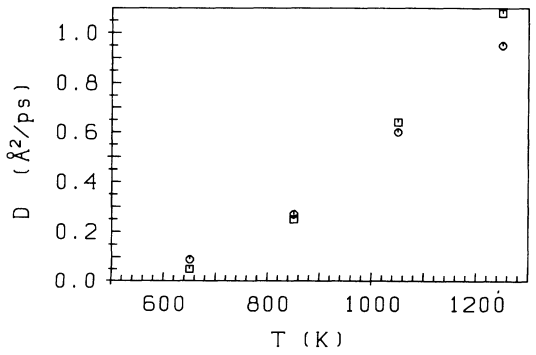

FIG. 9. Diffusion coefficient for liquid and supercooled liquid Ge as a function of temperature: ○ as derived from the mean-square displacements, □ calculated from the integral over the velocity-autocorrelation function $\psi(t)$.

B. Collective dynamics

The velocity autocorrelation functions shown in Fig. 10 also carry information on the collective dynamics of the system. For a purely Brownian motion $\psi(t)$ is monotonously decreasing. For ℓ-Ge the monotonic (diffusive) part is superposed by an oscillation of a period of about 0.2 ps, but the first few oscillations remain positive. This distinguishes ℓ-Ge from ℓ-Ar or ℓ-Na, where $\psi(t)$ becomes negative already at the first oscillation. The negative values of $\psi(t)$ show the importance of the caging effect of the neighboring atoms over the purely diffusive motion, the long-range oscillations are characteristic for metallic bonding as compared to van der Waals bonding in the rare-gas fluids.[82] Our results show that in ℓ-Ge the metallic bonding effects are clearly visible, but due to the rather loose packing the diffusive motion dominates over the caging effect. The Fourier transform of $\psi(t)$ defines the spectrum of the autocorrelation function,

$$\psi(\omega) = \int_0^\infty \psi(t)\, \cos(\omega t)\, dt \ . \tag{34}$$

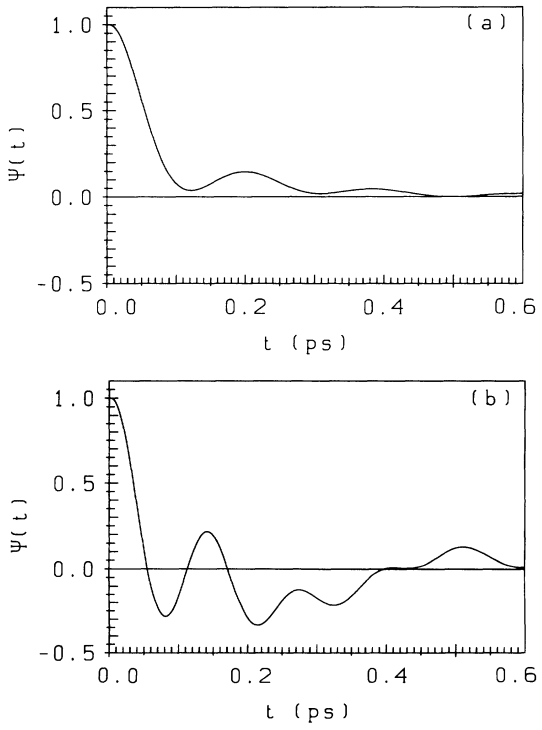

FIG. 10. Velocity-autocorrelation function for liquid (a) and annealed (b) amorphous Ge.

$\psi(\omega)$ is shown in Fig. 11. Besides the low-frequency diffusive modes one identifies an inelastic side peak at $\hbar\omega \sim 30$ meV, which is clearly related to the longitudinal acoustic modes in amorphous and crystalline Ge (see also below). The identification of these modes with longitudinal density fluctuations is in the spirit of the "diffusion-Umklapp model" for the dynamics of liquid and amorphous materials[83,84] and is certainly more realistic than their assignment to transverse optic vibrations (note that the stiffness of the bond angles is greatly reduced in the metallic liquid and that shear modes are more strongly damped than collective density fluctuations).

Figure 10(b) shows the velocity autocorrelation function for amorphous Ge. The diffusive background has disappeared, the complex time dependence of $\psi(t)$ arises from the superposition of several characteristic eigenfrequencies. After correction for the phonon-occupation function $n(\omega)$, the spectrum of the velocity autocorrelation function may be compared with the vibrational DOS $G(\omega)$ determined from neutron-inelastic scattering experiments[85,86] $[G(\omega) = \psi(\omega)\frac{1}{n(\omega)+1}]$. Figure 12 shows the result of the *ab initio* MD simulation for annealed amorphous Ge, compared with experimental data[85] on highly ordered and disordered *a*-Ge. The four peaks and shoulders in the calculated spectrum correspond (in the sequence of increasing energies) to the TA, LA, LO, and TO eigenmodes of polycrystalline Ge. The spectrum is in really good agreement with experiment.

We have also investigated the effect of the local order on the vibrational DOS. If the average for $\psi(t)$ is performed only over the subensemble of the fourfold coordinated sites, the changes in $G(\omega)$ correspond exactly to the differences observed between the disordered and the highly-ordered samples. Compared to the vibrational spectrum of amorphous metals,[87] the vibrational DOS of *a*-Ge shows much more distinctive features reminiscent of the crystal. This reflects the higher degree of local order.

VI. DEFECTS

The characteristic defects in *a*-Si and *a*-Ge are believed to be undercoordinated atoms,[88] usually referred to as "dangling bonds." The view is based on the interpretation of the electron paramagnetic resonance signal (EPR). Recently, this view has been challenged and it has been suggested[89] that the EPR-active center can also be a fivefold coordinated site with an electron state described as a "floating bond." Computer experiments based on classical many-body forces show that, depending on the way the amorphous sample is prepared, threefold and fivefold coordinated defects are found in varying concentrations.[21,22,24,90] In the most recent *ab initio* MD simulations of *a*-Si, only fivefold (T_5) defects have been found,[29] but in earlier runs[91] threefold (T_3) defects were detected as well.

In our study, we found that a purely geometrical definition of a defect is insufficient, but bonding and spectral properties must be considered as well. Due to fluctuation of the local defects already discussed in Sec. III, we found it most convenient to do the defect analysis for $T = 0$ configurations. Two different configurations where generated by slow and fast quenching after annealing (see Sec. III), the pair-correlation functions for both configurations are shown in Fig. 13. Overall the agreement between both configurations is rather good, the number of defects is definitely larger for the first configuration (prepared by a slow quench), but this configuration shows

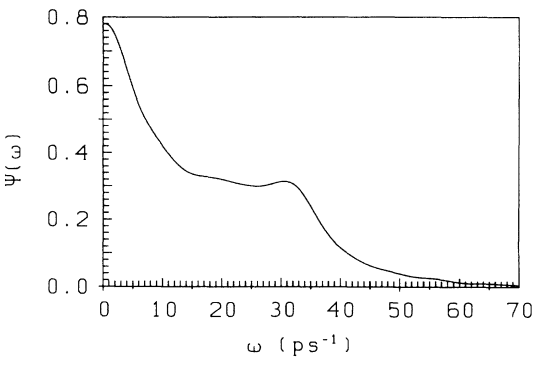

FIG. 11. Spectrum of the velocity autocorrelation function $\psi(\omega)$ for liquid Ge at $T = 1250$ K.

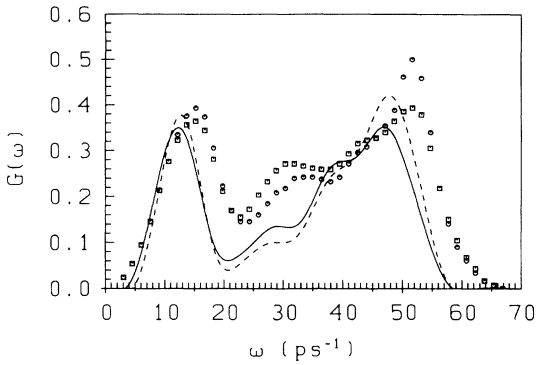

FIG. 12. Vibrational density of states $G(\omega)$ for annealed amorphous Ge. The solid line represents the *ab initio* MD result, the dashed line the DOS for the subensemble of the fourfold coordinated sites (cf. text). The squares and circles show the experimental results for disordered and highly-ordered samples (after Ref. 85).

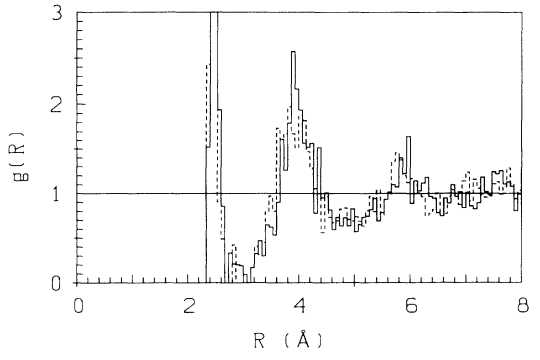

FIG. 13. Pair correlation function $g(R)$ for two *a*-Ge models at $T = 0$ K generated by quasi-Newton quenches, full line—configuration 1, dashed line—$T = 0$ configuration 2.

better agreement with experiment for $g(R)$ at large distances. Interestingly a number of atoms are for both configurations located in the minimum between the first and second peak of the pair-correlation function.

A. Geometrical defects

To characterize geometrical or coordination defects, one has to define the maximum length R_m of a nearest-neighbor bond. Because the minimum in $g(R)$ is not sharply defined for our a-Ge models (cf. Figs. 8 and 13), even a small change of R_m may fundamentally change the results of the analysis. This is demonstrated in Table V for both a-Ge models generated by the quasi-Newton quench. If the bond length is fixed at $R_m = 2.8$ Å, we find three T_3 and seven T_5 defects after the slow quench, and four T_3 and two T_5 defects after the fast quench. If R_m is increased to 3.0 Å there are no T_3 sites and we count 14 T_5 defects after the slow quench, and two T_3 and eight T_5 after the fast quench. Atom number 18 that has first been described as T_3, is now considered to be T_5. It is significant that the bond angles around both types of defects are reduced and have a broader distribution. For T_3 sites the average bond angle is $\Theta = 100.8$, i.e., considerably smaller than the tetrahedral bond angle and only slightly larger than the bond angle in threefold-coordinated As ($\Theta = 97.2°$).

B. Bonding defects

Evidently, a purely geometrical characterization of defects is insufficient. The tetrahedral sp^3 bond of the crystalline semiconductors is characterized by the bond charges placed in the midbond position. The bond charge may be visualized by plotting the electron density. Figure 14(a) shows the electron density for a slightly distorted tetrahedral configuration. The bond charges along the four bonds are clearly visible. Figure 14(b) shows the charge distribution around atom No. 55 in configuration 2, i.e., one of the two genuine T_3 sites. The atoms are arranged in the form of a trigonal prism with well-defined bond to the three neighbors of the central atom. A diffuse charge accumulation in the direction of the back bonds is all that can be seen of a "dangling bond." Figures 14(c), 14(d), and 14(e) show three T_5 sites (atoms No. 20, 36, and 63). T_5 sites tend to have 3 or 4 "strong" and 2 or 1 "weak" bonds: if an additional atom is squeezed into the tetrahedral configuration the distortion weakens the bonds closest to the added atom. Only exceptionally we find a T_5 site with five equally strong bonds [Fig. 14(e)]. The existence of a bond charge depends very critically on the length of the bond: for $d_1 \geq 2.85$ Å no bond charges have been found. Therefore, $R_m = 2.8$ Å for the maximum bond length leads to a physically more meaningful definition of defects than the pure geometrical definition in terms of the position of the minimum in $g(R)$. The small hump in the minimum of $g(R)$ contains most of the weak bonds of the T_5 defects. A particularly interesting feature is found in the charge distribution around atom No. 18 [see Fig. 14(f)]. The site is described as T_3 or T_5, depending on the assumption on the maximum length of a nearest-neighbor bond. The bonds to the two more distant neighbors are very weak and the three remaining bonds are nearly coplanar, i.e., the bond angles are considerably strained. Only two of the bonds

TABLE V. Structural characteristics of tetrahedrally coordinated (T_4) and of defect (T_3, T_5) sites in two a-Ge models generated by quasi-Newton quenches.

$R_m = 2.8$ Å	%	d_1 (Å)	Δd_1 (Å)	Θ (deg)	$\Delta\Theta$ (deg)
Model 1 (slow quench)					
T_3	4.7	2.52	0.12	100.2	19.8
T_4	84.4	2.47	0.06	108.8	13.5
T_5	10.9	2.56	0.11	103.5	24.4
Model 2 (fast quench)					
T_3	6.3	2.44	0.04	107.2	18.1
T_4	90.6	2.45	0.06	108.7	13.9
T_5	3.1	2.57	0.07	105.7	26.2
T_3 : Atom Nos. 1, 18, 39, 55					
T_5 : Atom Nos. 61, 63					

$R_m = 3.0$ Å	%	d_1 (Å)	Δd_1 (Å)	Θ (deg)	$\Delta\Theta$ (deg)
Model 1 (slow quench)					
T_3	0				
T_4	78.1	2.46	0.07	108.9	13.0
T_5	21.9	2.59	0.15	104.1	25.3
Model 2 (fast quench)					
T_3	3.1	2.44	0.03	100.3	16.6
T_4	84.4	2.45	0.06	108.6	13.6
T_5	12.5	2.58	0.14	103.7	25.7
T_3 : Atom Nos. 39, 55					
T_5 : Atom Nos. 15, 18, 20, 36, 40, 52, 61, 63					

have well-defined bond charges, the third bond is rather asymmetric, with most of the charge concentrated on the central atom. We shall see in a moment, that this defect has peculiar spectral properties.

C. Spectral defects

Of greatest importance for the electronic properties of amorphous semiconductors are the spectral defects, i.e. the defects giving rise to states in the gap. The recent work of Drabold *et al.*[68] has shown that a geometrical defect is neither a necessary nor a sufficient condition for the existence of a spectral defect. We have analyzed the one-electron states in the gap by analyzing their electron density distributions and localization properties. To study localization we have subdivided the MD cell into a grid of $M = m^3$ small cubes. The localization parameter L is defined as

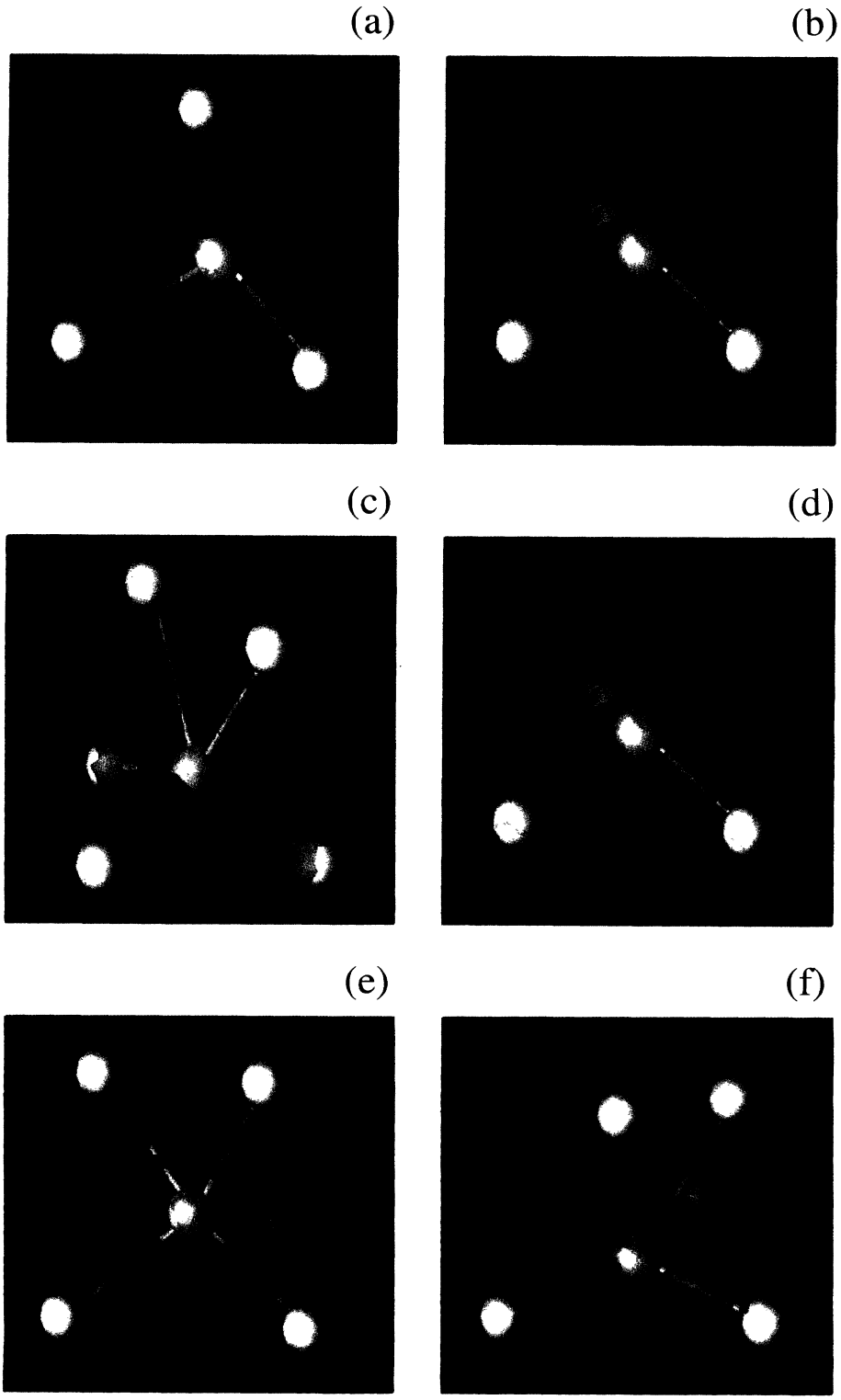

FIG. 14. Analysis of defects in a-Ge in terms of electron density plots. The geometry of the nearest-neighbor group of atoms is shown by a ball-and-stick model, the electron density is represented by a contor plot with the light blue areas having the highest electron density. Only the charge distribution along nearest-neighbor bonds is shown, the rest has been clipped. (a) Slightly distorted tetrahedral T_4 site; (b) threefold coordinated T_3 defect; (c), (d) and (e) two characteristic T_5 sites, (f) atom No. 18, T_3, or T_5 depending on cutoff distance.

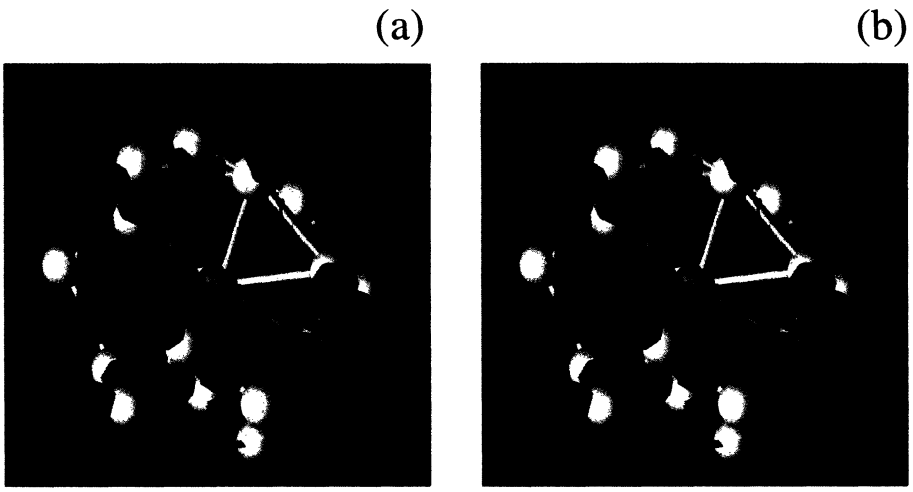

FIG. 15. (a) Electron density of band 128 in the vincinity of atom No. 18 (yellow ball). (b) Total electron density in the vincinity of atom No. 18; see text.

$$L = \frac{\sum_{i=1}^{M} q_{i,n}}{M \sum_{i=1}^{M} q_{i,n}^2}, \tag{35}$$

where $q_{i,n}$ is the charge contained in the ith cell for the nth band. If the charges are normalized according to $\sum_i q_{i,n} = 1$, $L \approx 1$ characterizes a completely extended state, and $L \approx 1/M$ a state localized within a single small cube. An analysis with $m = 8, 16, 32$ for the quenched configuration 2 shows that the highest occupied state ($n = 128$) is distinctly more localized than all other states (occupied or empty). Indeed the charge density corresponding to this state is concentrated in a single charge density maximum close to atom No. 18. This is shown in Fig. 15. Part (b) shows the total electron density in the vicinity of this site: it is evident that atom 18 together with its two neighbors forming long bonds forms an isosceles triplet and that this "metallic configuration" is characterized by the absence of covalent bond charges. Part (a) of the figure shows the electron density for band No. 128 only: the charge is concentrated in the direction of the third weak bond of atom 18 [the "asymmetric" bond of Fig. 14(f)].

This shows that while we have a relatively large number of geometrical defects in this configuration, they create only a single localized state. This state is associated with a strong local perturbation of tetrahedral bonding, not only a coordination defect, but in addition, a very strong strain on nearly all bond angles.

However, we have to remember that even small fluctuations in the atomic geometry can induce relatively large changes in the spectrum, especially in the states situated in the energy gap.[68] This is illustrated in Fig. 16 where we show the time evolution (at $T = 300$ K) of the electronic eigenvalues close to the gap. It is evident that the states in the gap show the largest fluctuation and these fluctuations are associated with formation and decay of localized states.

The *ab initio* MD simulation offers the possibility of investigating these important phenomena. Here we have merely touched the problem and shown that it has become tractable. Future work will be needed in order to assess the local defects that are really characteristic for amorphous semiconductors and their spectral properties.

VII. SUMMARY AND CONCLUSIONS

We have presented an *ab initio* study of the liquid-metal–amorphous-semiconductor transition in Ge. Our calculation is based on a novel variant of density-functional molecular dynamics that allows us to perform simulations for metallic systems with perfect control of adiabaticity while correctly describing occupied and empty states on both sides of the Fermi level. Our approach is based on finite-temperature local-density functional theory, direct energy minimization using a preconditioned conjugate gradient technique, very accurate pseudopotentials, and on Nosé dynamics for simulating a canonical ensemble. Although we perform an exact energy minimization after each MD step, our technique is at least as efficient as CP calculations: the time step is larger than a typical CP-time step by a factor of 10

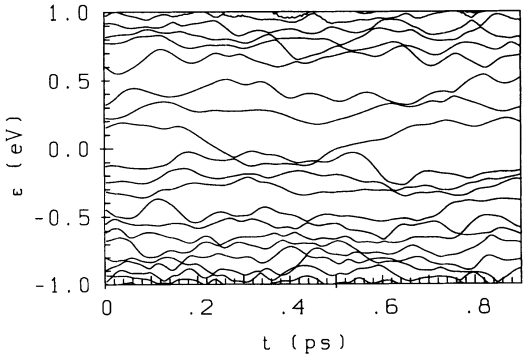

FIG. 16. Fluctuations of the one-electron energies ϵ_i in the vicinity of the Fermi level ($\epsilon = 0$) as a function of time at $T = 300$ K.

– 20, each energy-minimization requires an average two to three conjugate-gradient steps (one CG step requiring about two times the CPU-time of one CP step). Hence there is a gain in computational efficiency by a factor of 1.5–2. To be specific, a 1 ps run for liquid Ge took about 16 h CPU on an SNI-Fujitsu S100.

The efficiency of our code allows us to perform relatively extended simulations. The overall length of our MD run (including the second cooling run) was 30 ps. This is sufficient to obtain an accurate description of the structural, dynamic, and electronic properties of liquid and amorphous Ge: our computer-generated data are in good agreement with neutron diffraction, inelastic neutron scattering, and photoemission data. Beyond the examination of properties accessible also to laboratory experiments, our computer experiments serve to investigate many-atom correlations, the geometrical bonding, and spectral properties of defects in the amorphous network. Our analysis shows that the computer-generated model contains both undercoordinated (T_3) or "dangling-bond" and overcoordinated (T_5) or "weak-bond" defects. We also find that a purely geometrical definition of a defect is not always meaningful—the analysis of the bonding and spectral properties gives a physically more meaningful picture.

Finally, we want to come back to the technical merit of our work. Based on developments published in a series of different papers, our technique assembles all the ingredients necessary for making *ab initio* MD calculations for metals as straightforward and reliable as CP calculations for semiconductors. The challenge is now to extend the approach to transition metals. We have recently completed a version of the code based on the use of ultrasoft pseudopotential making *ab initio* MD simulations for transition metals feasible.[92]

Note added in proof. We recently became aware that the self-diffusion coefficient of liquid Ge has been measured by P. V. Pavlov and E. V. Dobrokhotov [Sov. Phys. Solid State **12**, 225 (1970)], using two different methods. The experimental values quoted by these authors are $D=1.21\times10^{-4}$ cm^2 s-1 and $D=0.78\times10^{-4}$ cm^2 s^{-1} close to the melting point, in reasonable agreement with $D_{\rm calc}=1.0\times10^{-4}$ au^2 s^{-1}. J. H. thanks Dr. I. L. Gavzóu for bringing this reference to his attention.

ACKNOWLEDGMENT

This work has been supported by Siemens-Nixdorf Austria within the contract with the Technische Universität Wien.

[1] See, for instance, S. R. Elliott, *Physics of Amorphous Materials* (Longman, London 1984); *Amorphous Materials: Modeling of Structure and Properties*, Conference Proceedings of the Metallurgical Society of AIME, edited by V. Vitek (AIME, New York 1983); N. E. Cusack, *The Physics of Structurally Disordered Matter* (Hilger, Bristol, 1987).

[2] See, e.g., *Investigations of Higher Order Correlation Functions*, edited by J. Suck, D. Quitmann, and B. Maier [J. Phys. (Paris) Colloq. **46**, C9 (1985)].

[3] D. E. Polk and D. S. Boudreaux, Phys. Rev. Lett. **31**, 92 (1973).

[4] F. Wooten and D. Weaire, Solid State Phys. **40**, 2 (1987).

[5] For simple-metal systems see, e.g., J. Hafner and S. S. Jaswal, Phys. Rev. B **37**, 7311 (1988); for transition-metal systems see Ch. Hausleitner and J. Hafner, *ibid.* **45**, 128 (1992); B **47**, 5689 (1993), and references cited therein.

[6] A. Baranyai, I. Ruff, and R. L. Mc Greevy, J. Phys. C **19**, 453 (1986); T. F. Soules, J. Chem. Phys. **71**, 4570 (1979).

[7] J. Hafner, *From Hamiltonians to Phase Diagrams* (Springer, Berlin, 1987).

[8] G. Etherington, A. C. Wright, J. T. Wenzel, J. C. Dore, J. H. Clarke, and R. N. Sinclair, J. Non-Cryst. Solids **48**, 265 (1982).

[9] J. Fortner and J. S. Lannin, Phys. Rev. B **39**, 5527 (1989).

[10] A. Georghiu, K. Driss-Khodja, S. Fisson, M. L. Theye, and J. Dixmier, J. Phys. (Paris) Colloq. **46**, C8-545 (1985).

[11] J. P. Gabathuler and S. Steeb, Z. Naturforsch. Teil A **34**, 1314 (1979).

[12] Y. Waseda, *The Structure of Non-Crystalline Materials—Liquids and Amorphous Solids* (McGraw-Hill, New York, 1981).

[13] C. Bergman, C. Bichara, P. Chieux, and J. P. Gaspard, J. Phys. (Paris) Colloq. **46**, C8-97 (1985).

[14] A. Arnold, N. Mauser, and J. Hafner, J. Phys. Condens. Matter **1**, 965 (1989).

[15] W. Jank and J. Hafner, Phys. Rev. B **41**, 1497 (1990).

[16] W. Jank and J. Hafner, J. Phys. Condens. Matter **1**, 4235 (1989).

[17] G. Kreuch and J. Hafner, Verh. Dtsch. Phys. Ges. **5**, 1357 (1993).

[18] F. H. Stillinger and T. A. Weber, Phys. Rev. B **31**, 5262 (1985).

[19] R. Biswas and D. R. Hamann, Phys. Rev. B **36**, 6434 (1987).

[20] J. Tersoff, Phys. Rev. B **37**, 6991 (1988).

[21] J. Q. Broughton and X. P. Li, Phys. Rev. B **35**, 9120 (1987).

[22] W. D. Luedtke and U. Landmann, Phys. Rev. B **37**, 4656 (1988); **40**, 1164 (1989).

[23] R. Biswas, G. S. Grest, and C. M. Soukoulis, Phys. Rev. B **36**, 7437 (1987).

[24] K. Ding and H. C. Andersen, Phys. Rev. B **34**, 6987 (1986).

[25] R. Car and M. Parrinello, Phys. Rev. Lett. **55**, 2471 (1985).

[26] W. Kohn and L. Sham, Phys Rev. **140**, A1133 (1965); W. Kohn, in *Highlights of Condensed Matter Theory*, edited by M. P. Tosi, M. Fumi, and F. Bassani (North-Holland, Amsterdam, 1985).

[27] I. Stich, R. Car, and M. Parrinello, Phys. Rev. Lett. **63**, 2240 (1989); Phys. Rev. B **44**, 4262 (1991).

[28] F. Buda, G. L. Chiarotti, I. Stich, R. Car, and M. Parrinello, J. Non-Cryst. Solids **114**, 7 (1989).

[29] I. Stich, R. Car, and M. Parrinello, Phys. Rev. B **44**, 11 092 (1991).

[30] G. Pastore, E. Smargiassi, and F. Buda, Phys. Rev. A **44**, 6334 (1991).

[31] S. Nosé, J. Chem. Phys. **81**, 511 (1984).

[32] P. E. Blöchl and M. Parrinello, Phys. Rev. B **45**, 9413 (1992).

[33] N. D. Mermin, Phys. Rev. **137**, A 1441(1965).
[34] G. Kresse and J. Hafner, Phys. Rev. B **47**, 558 (1993).
[35] G. Kresse and J. Hafner, J. Non-Cryst. Solids **117 & 118**, 956 (1993).
[36] We use the parametrization presented by J. P. Perdew and A. Zunger, Phys. Rev B **23**, 5048 (1981).
[37] M. Weinert and J. W. Davenport, Phys. Rev. B. **45**, 13 709 (1992).
[38] R. M. Wentzcovitch, J. L. Martins, and P. B. Allen, Phys. Rev B **45**, 11 372 (1992).
[39] M. P. Teter, M. C. Payne, and D. C. Allan, Phys. Rev. B **40**, 12 255 (1989).
[40] R. D. King-Smith, M. C. Payne, and J. S. Lin, Phys. Rev B **44**, 13 063 (1991).
[41] T. A. Arias, M. C. Payne, and J. D. Joannopoulos, Phys. Rev. B **45**, 1538 (1992).
[42] M. C. Payne, M. P. Teter, D. C. Allan, T. A. Arias, and J. D. Joannopoulos, Rev. Mod. Phys. **64**, 1045 (1992).
[43] D. M. Bylander, L. Kleinman, and S. Lee, Phys. Rev. B **42**, 1394 (1990); D. M. Bylander and L. Kleinman, *ibid.* **45**, 9663 (1992).
[44] D. Vanderbilt, Phys. Rev. B **32**, 8412 (1985).
[45] G. Kresse, J. Hafner, and R. J. Needs, J. Phys. Condens. Matter **4**, 7451 (1992).
[46] A. De Vita, Ph.D. thesis, Keele University, 1992; A. De Vita and M. J. Gillan (unpublished).
[47] I. Stich, R. Car, M. Parrinello, and S. Baroni, Phys. Rev. B **39**, 4997 (1989).
[48] M. J. Gillan, J. Phys. Condens. Matter **1**, 689 (1989).
[49] G. P. Kerker, Phys. Rev. B **23**, 3082 (1981).
[50] D. M. Bylander and L. Kleinman, Phys. Rev. B **46**, 13 756 (1992).
[51] S. Nosé, Prog. Theor. Phys. Suppl. **103**, 1 (1991).
[52] C. W. Gear, *Numerical Initial Value Problem in Ordinary Differential Equations* (Prentice Hall, Englewood Cliffs, NJ, 1971), Chaps. 9 and 10.
[53] G. Kresse, Ph.D. thesis, Technische Universität Wien, 1993.
[54] G. B. Bachelet, D.R. Hamann, and M. Schlüter, Phys. Rev. B **26**, 4199 (1982).
[55] N. Troullier and J. L. Martins, Phys. Rev. B **43**, 1993 (1991).
[56] A. M. Rappe, K. M. Rabe, E. Kaxiras, and J. D. Joannopoulos, Phys. Rev. B **41**, 1227 (1990).
[57] A. Garcia, C. Elsässer, J. Zhu, and S. G. Louie, Phys. Rev. B **46**, 9829 (1992).
[58] M. T. Yin and M. L. Cohen, Phys. Rev. B **26**, 5668 (1982).
[59] E. Wigner, Phys. Rev. **133**, 1002 (1934).
[60] L. Kleinman and D. M. Bylander, Phys. Rev. Lett. **48**, 1425 (1982).
[61] P. Viščor, J. Non-Cryst. Solids **101**, 156 (1988).
[62] G. A. N. Cornell and R. J. Temkin, Phys. Rev. B **9**, 5323 (1974).
[63] D. L. Evans, M. P. Teter, and N. F. Borelli, J. Non-Cryst. Solids **17**, 245 (1975).
[64] D. Beeman and B. L. Bobbs, Phys. Rev. B **12**, 1399 (1975).
[65] D. Henderson, J. Non-Cryst. Solids **16**, 317 (1974).
[66] P. Steinhardt, R. Alben, and D. Weaire, J. Non-Cryst. Solids **15**, 199 (1974).
[67] P. Pulay, in *Modern Theoretical Chemistry*, edited by H. F. Schaefer (Plenum, New York, 1977); Mol. Phys. **17**, 197 (1969).
[68] D. A. Drabold, P. A. Fedders, S. Klemm, and O. F. Sankey, Phys. Rev. Lett. **67**, 2179 (1991).
[69] W. H. Press, B. P. Flannery, S. A. Teukolsky, and W. T. Vetterling, *Numerical Recipes: The Art of Scientific Computing* (Cambridge University Press, Cambridge 1986); we use an implementation similar to the schemes discussed by S. Blügel, Ph.D. thesis, Aachen University, 1988.
[70] F. H. Stillinger and T. A. Weber, J. Chem. Phys. **80**, 4434 (1984).
[71] J. Hafner, J. Phys. F **18**, 153 (1988).
[72] A. Baldereschi, Phys. Rev. B **7**, 5212 (1973); H. J. Monkhorst and J. D. Pack, Phys. Rev. B **13**, 5188 (1976).
[73] J. Hafner and G. Kahl, Solid State Commun. **49**, 1125 (1981); J. Phys. F **14**, 2259 (1984).
[74] W. Jank and J. Hafner, Europhys. Lett. **7**, 623 (1988).
[75] G. Indlekofer, P. Oelhafen, R. Lapka, and H. J. Güntherodt, Z. Phys. Chem. **157**, 465 (1988).
[76] A. Ferrante and M. P. Tosi, J. Phys. Condens. Matter **1**, 1679 (1989).
[77] J. P. Gaspard, Ph. Lambin, C. M. Moutet, and J. P. Vigneron, Philos. Mag. B **50**, 103 (1984).
[78] F. Spaepen and D. Turnbull, in *Laser Processing of Semiconductors*, edited by J. M. Poate and J. W. Mayer (Academic, New York 1982), p. 15.
[79] C. Senemaud, E. Belin, A. Gheorghiu, and M. L. Theye, J. Non-Cryst. Solids **77**, 1289 (1985).
[80] L. Ley, S. Kowalczyk, R. Pollak, and D. A. Shirley, Phys. Rev. Lett. **29**, 1088 (1972).
[81] J. D. Joannopoulos and M. L. Cohen, Solid State Phys. **31**, 71 (1976).
[82] C. L. Croxton, *Liquid State Physics* (Cambridge University Press, Cambridge, 1974), p. 243.
[83] J. Jäckle and K. Froböse, J. Phys. F **7**, 2331 (1977).
[84] J. Hafner, J. Phys. C **14**, L278 (1981).
[85] N. Maley, J. S. Lannin, and D. L. Price, Phys. Rev. Lett. **56**, 1720 (1986).
[86] W. A. Kamitakahara, C. M. Soukoulis, H. R. Shanks, O. Buchenau, and G. S. Grest, Phys. Rev. B **36**, 6539 (1987).
[87] See, e.g., J. Hafner, J. Phys. C **16**, 5773 (1983).
[88] See, e.g., the articles of M. H. Brodsky *et al.*, and R. A. Street and D. K. Biegelsen in *The Physics of Hydrogenated Amorphous Silicon II*, edited by J. D. Joannopoulos and G. Lucovsky (Springer, Berlin, 1984).
[89] S. T. Pantelides, Phys. Rev. Lett. **57**, 2979 (1986).
[90] I. Kwon, R. Biswas, G. S. Grest, and C. M. Soukoulis, Phys. Rev. B **41**, 3678 (1990).
[91] I. Stich, Ph.D. thesis, SISSA Trieste, 1989.
[92] G. Kresse and J. Hafner, Phys. Rev. B **48**, 13 115 (1993).

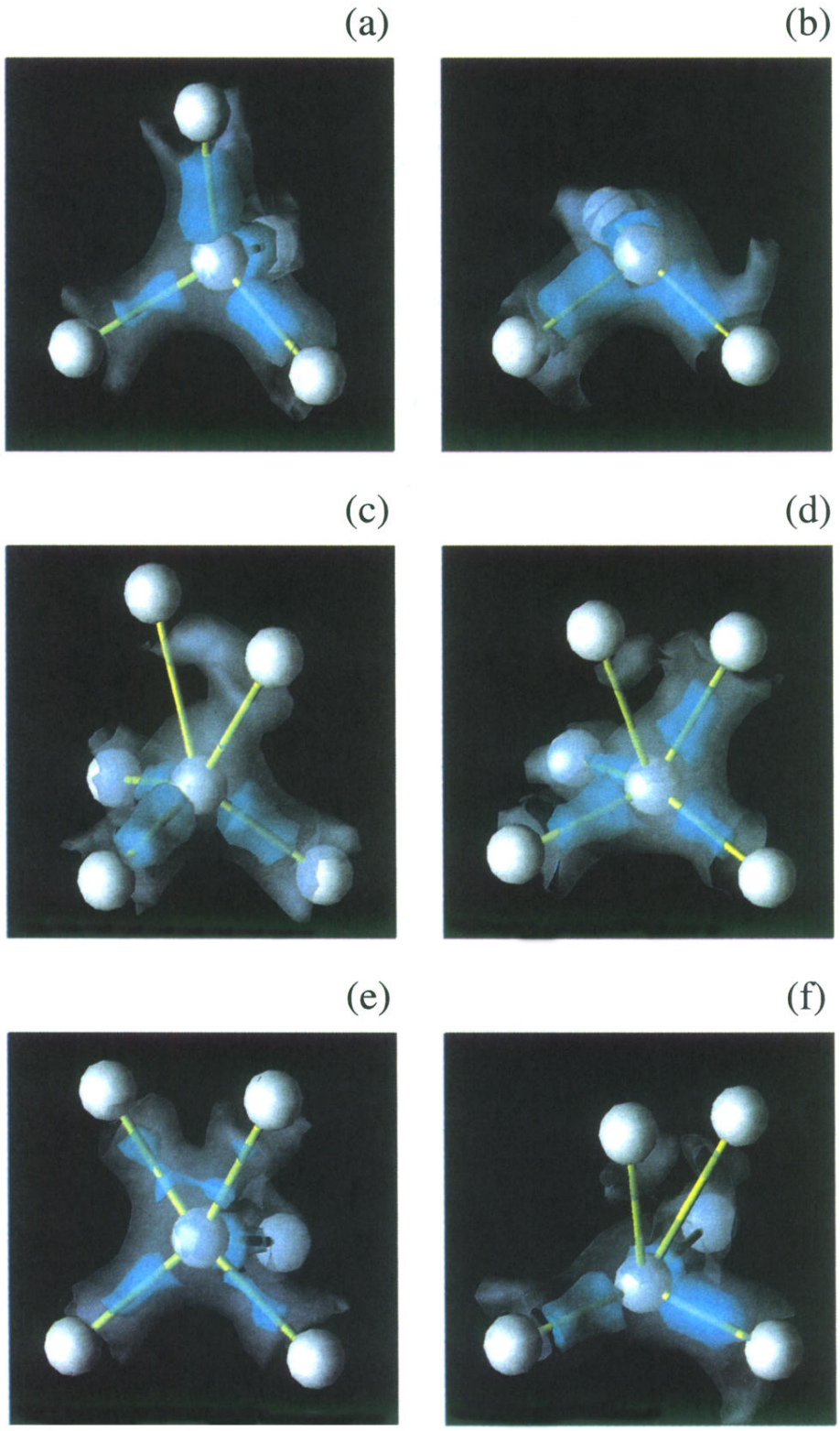

FIG. 14. Analysis of defects in a-Ge in terms of electron density plots. The geometry of the nearest-neighbor group of atoms is shown by a ball-and-stick model, the electron density is represented by a contor plot with the light blue areas having the highest electron density. Only the charge distribution along nearest-neighbor bonds is shown, the rest has been clipped. (a) Slightly distorted tetrahedral T_4 site; (b) threefold coordinated T_3 defect; (c), (d) and (e) two characteristic T_5 sites, (f) atom No. 18, T_3, or T_5 depending on cutoff distance.

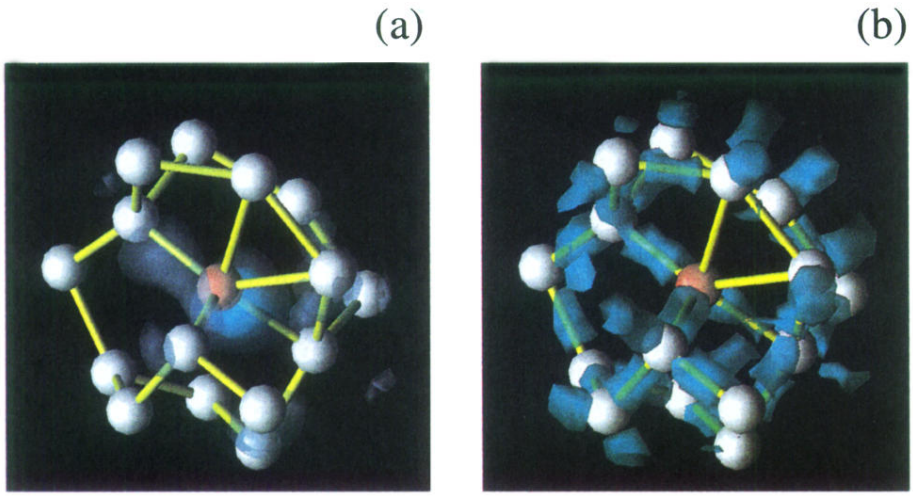

FIG. 15. (a) Electron density of band 128 in the vincinity of atom No. 18 (yellow ball). (b) Total electron density in the vincinity of atom No. 18; see text.